BMC Medicine

RESEARCH

Open Access

Methylmalonate accumulation contributes to myocardial vulnerability post-reperfusion: a novel therapeutic target and prognostic biomarker

Shanjie Wang[1,2†], JunChen Guo[1,2†], Zeng Wang[1,2†], Kegong Chen[3†], Xiaoxuan Liu[1,2], Yan Cui[4], Ye Wang[1,2], Zhaoying Li[1,2], Hengxuan Cai[1,2], Guanpeng Ma[1,2], Zhenming Zhang[1,2], Guokun Wang[1,2], Lili Xiu[1,2], Shuijie Li[2,5], Hulun Li[6], Haibo Jia[1,2*], Bo Yu[1,2*] and Shaohong Fang[1,2,3*]

Abstract

Background Dysfunctional mitochondria are a prominent feature of myocardial ischemic-reperfusion (I/R) injury, but the clinical translation is scarce. Congenital dysbolism methylmalonic acidemia causes fatal mitochondrial lesions and premature death. However, the biological impact of mitochondrial metabolite methylmalonic acid (MMA) in the pathogenesis of I/R and its translational relevance were unknown.

Methods MMA and relevant metabolites were measured in 3 independent human cohorts and animals. Cardiac *Mmut*-conditional knockout (endogenous MMA elevation) and exogenous MMA administration were conducted in mouse I/R model. The potential mechanism was explored through multiomics, chromatin immunoprecipitation, and site-directed mutagenesis assays. The translational value of targeting MMA metabolism was assessed in a porcine I/R model.

Results Circulating MMA predicts myocardial injury or heart failure risk post-reperfusion, which outmatches its isomer succinate in humans. Both MMA and succinate were elevated in heart tissues of mice at the initial period post-I/R, while later, MMA maintained higher levels, but succinate rapidly decreased to baseline levels. Endogenous and exogenous MMA, not succinate, increased susceptibility to myocardial I/R injury and mitochondrial dyshomeostasis, including impaired mitochondrial bioenergetics, biogenesis, and renovation. Mechanistically, MMA elevation inhibited the deacetylase activity of SIRT1; thus, hyperacetylation of transcription factor CREB^{K309} blunted its binding to the BNIP3 promoter and inhibited BNIP3-mediated mitochondrial quality control. Adeno-associated virus

†Shanjie Wang, JunChen Guo, Zeng Wang, and Kegong Chen contributed equally to this work.

*Correspondence:
Haibo Jia
jhb101180@163.com
Bo Yu
yubodr@163.com
Shaohong Fang
fangshaohong@hrbmu.edu.cn
Full list of author information is available at the end of the article

© The Author(s) 2025. **Open Access** This article is licensed under a Creative Commons Attribution-NonCommercial-NoDerivatives 4.0 International License, which permits any non-commercial use, sharing, distribution and reproduction in any medium or format, as long as you give appropriate credit to the original author(s) and the source, provide a link to the Creative Commons licence, and indicate if you modified the licensed material. You do not have permission under this licence to share adapted material derived from this article or parts of it. The images or other third party material in this article are included in the article's Creative Commons licence, unless indicated otherwise in a credit line to the material. If material is not included in the article's Creative Commons licence and your intended use is not permitted by statutory regulation or exceeds the permitted use, you will need to obtain permission directly from the copyright holder. To view a copy of this licence, visit http://creativecommons.org/licenses/by-nc-nd/4.0/.

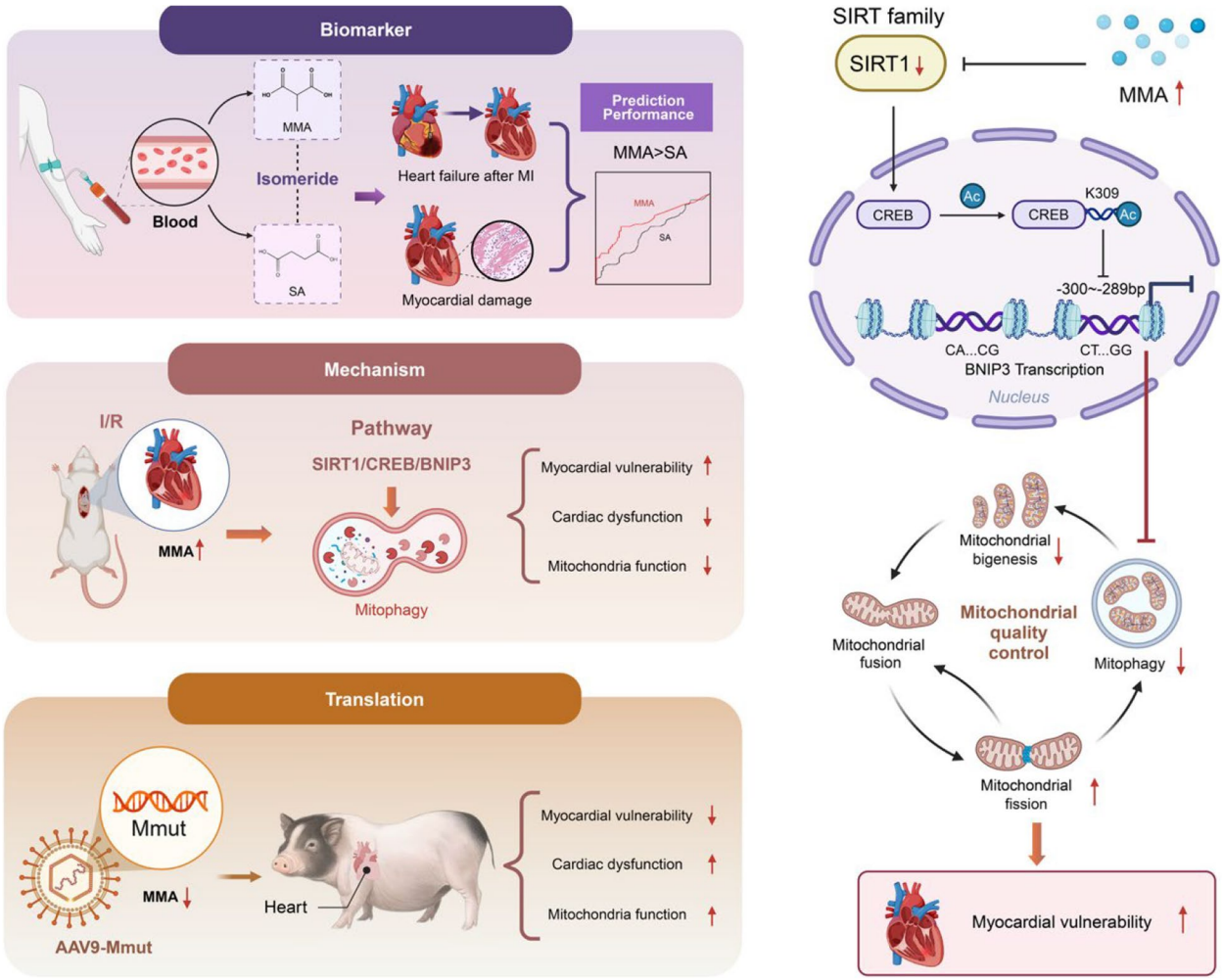
9-containing *MMUT* gene delivery ameliorated impaired MMA metabolism to improve mitochondrial quality and cardiac phenotypes in I/R pigs.

Conclusions This study revealed an unrecognized harmful effect of MMA on myocardial vulnerability distinct from its isomer succinate. Targeting MMA metabolism represents a promising strategy to optimize risk stratification and mitigate myocardial injury in patients with AMI.

Keywords Myocardial ischemia/reperfusion injury, Mitochondria, Methylmalonate, Methylmalonic acid, MMA, Succinic acid, Succinate, SA, Translation

Graphical Abstract

Compared with its well-known isomer succinate, the mitochondria-derived metabolite MMA is more robustly associated with myocardial injury post-reperfusion in both humans and animals. An increase in MMA but not succinate increased myocardial susceptibility and mitochondrial dysfunction under I/R conditions via inhibiting SIRT1/CREB/BNIP3-mediated mitochondrial quality control. In large animal experiments, promoting MMA metabolism through in vivo injection of AAV9-containing MMUT significantly mitigated the infarct size, mitochondrial dysfunction, and cardiac remodeling post-I/R. HF, heart failure; MI, myocardial infarction; CVD, cardiovascular disease.



Key question(s)

Methylmalonic acid (MMA) causes fatal mitochondrial damage and premature death in patients with congenital methylmalonic acidemia. However, can mitochondrial MMA metabolism serve as a promising target to alleviate myocardial I/R injury characterized by mitochondrial dysfunction?

Key finding(s)

- MMA elevation predicts myocardial injury or HF risk post-MI and reperfusion in humans and animals.
- Cardiac MMA maintains higher levels post-IR, whereas its isomer succinate rapidly decreases to baseline levels after early elevation.
- MMA but not succinate amplifies myocardial susceptibility in I/R mice by disturbing SIRT1/CREB^{K309}/BNIP3-mediated self-regulation of mitochondrial quality control.
- Improving MMA metabolism alleviates infarct size and adverse remodeling in a pig I/R model.

Take home message

Targeting mitochondrial MMA metabolism represents a promising strategy to mitigate myocardial injury in patients with AMI and reperfusion.

Translational perspective

This study elucidates that MMA elevation represents an unheeded feature and contributor to prolonged myocardial reperfusion injury in both humans and animals that is distinct from its isomer succinate, expanding the clinical relevance of mitochondrial MMA metabolism from inherited disease to the management of cardiovascular disease. Targeting mitochondrial MMA metabolism represents a promising therapeutic strategy for restoring mitochondrial quality and mitigating myocardial injury in patients with AMI and reperfusion.

Background

Acute myocardial infarction (AMI) and subsequent heart failure (HF) remain major causes of morbidity and mortality worldwide [1]. Despite the undeniable benefits of primary percutaneous coronary intervention (pPCI), reperfusion causes additional cardiomyocyte death, accounting for a half of the final infarct area, termed myocardial ischemia/reperfusion (I/R) injury [2]. Healthy and damaged mitochondria have been shown to play opposite roles as arbiters of myocardial fate after I/R [3]. Mitochondrial quality control is an indispensable mechanism for preserving mitochondrial homeostasis in response to stress [4, 5]. The I/R process is accompanied by significant alterations in mitochondrial metabolism; however, its impact on myocardial vulnerability remains largely unexplored [6].

Methylmalonic acid (MMA), a mitochondrial intermediate metabolite, is allosteric to succinate and enters the Krebs cycle via the mitochondrial enzyme MMUT and the coenzyme vitamin B12 [7, 8]. In children, congenital methylmalonic acidemia, which is caused primarily by MMUT mutation, is characterized by pathologically vacuolated megamitochondria and lethal damage to the mitochondria-rich brain and kidney. Numerous experimental studies have revealed that MMA disturbs mitochondrial energy metabolism and induces excessive reactive oxygen species (ROS) generation in neurons and renal tubular epithelial cells [9]. However, the impact of MMA on the cardiovascular system remains largely unknown. Only a few recent case studies have reported congenital heart disease and HF as rare manifestations of inborn methylmalonic acidemia [10, 11]. These findings from genetic studies may provide clues for the management of cardiovascular disease characterized by mitochondrial damage [12]. Our cohort studies recently revealed that mitochondrial metabolite MMA is positively associated with cardiovascular mortality risk independent of coenzyme vitamin B12 among adults with or without cardiometabolic disease [8, 13]. Moreover, MMA improves the reclassification of the Framingham risk score for 10-year mortality in patients with cardiovascular disease (CVD), surpassing the performance of C-reactive protein and homocysteine [8]. These clinical clues prompted our investigation into whether MMA is implicated in myocardial vulnerability post-I/R. Subsequently, we sought to determine whether mitochondrial MMA metabolism could be considered a potential therapeutic target for cardioprotection.

In this study, we found that MMA accumulation was significantly associated with the extent of myocardial injury and incident HF after AMI in humans compared with its isomer succinate and coenzyme vitamin B12. We established murine and porcine myocardial I/R injury models with cardiac MMUT knockout or overexpression to investigate the role of MMA accumulation in the pathogenesis and mechanisms of myocardial vulnerability and to evaluate the translational relevance.

Methods

Human studies

The population-based analysis (cohort 1) was based on the US National Health and Nutrition Examination Survey (NHANES) 1999–2004 [14]. The NHANES is a nationally representative survey with an ongoing, stratified, multistage sampling design used to assess the health and nutritional status of the noninstitutionalized civilian population of the USA. The NHANES was approved by

the research ethics review board of the Centers for Disease Control and Prevention (Protocol No. 98–12); all participants provided informed consent. Serum MMA and cardiac biomarkers were measured in three 2-year study cycles (1999–2000, 2001–2002, and 2003–2004). Among 31,126 participants in NHANES 1999–2004, we excluded individuals under the age of 18 ($n=14,065$), pregnant women (identified by self-report and HCG test, $n=848$), those with a history of cardiovascular diseases (a self-reported diagnosis of coronary heart disease, congestive heart failure, or stroke by physicians, $n=1888$), and participants without eligible assessment for circulating MMA ($n=1824$) and high-sensitivity cTn ($n=1091$). A total of 11,410 adults were included in the analysis. The detailed information has been described in our previous studies [15, 16].

The hospital-based study (cohort 2) included 98 patients who were diagnosed with AMI at 18 years of age or older; this subset of patients from the prospective multicenter hospital-based AMI cohort supported by the Chinese 13·5 National Key Program for Health and Chronic Disease Management started in 2017 [17]. All patients with chest pain admitted to the emergency department were screened for suspected acute coronary syndrome by the attending clinician. AMI was diagnosed as (1) persistent chest pain within 12 h of symptom onset; (2) new ST-segment depression, T wave flatness/inversion, ST-segment elevation of 0.1 mV or greater in two or more adjacent leads, new left bundle-branch block, or dynamic electrocardiogram variations; and (3) troponin cTnI (>0.3 ng/mL) or creatine kinase isoenzyme-MB (>5 ng/mL) greater than the 99th percentile of the normal reference value. The definition of HF was based mainly on the Framingham study and 2016 ESC guidelines [5, 6]. Blood samples were collected from all participants after admission. In cohort 2, 362 AMI survivors at discharge participated in the program between September 2017 and December 2017 from Harbin Medical University Second Affiliated Hospital, Harbin, China. During the 1-year follow-up after discharge, 7 patients were lost to follow-up, 12 participants died without heart failure (HF), 49 patients with incident HF, and 16 patients with re-MI or stroke were recorded. AMI patients free of incident HF or other cardiovascular events were treated as controls. A propensity score matching approach was used to balance the baseline differences between the two groups. Participants without HF were selected via the nearest neighbor matching algorithm and 1:1 nonreplacement method with a caliper size of 0.2 standard deviation of the logit of the propensity score [18], including age, sex, BMI, MI type, diabetes status, dyslipidemia status, and coronary stenosis score. Blood samples were collected and retained in the Biobank of the Key Laboratory of Myocardial Ischemia, Ministry of Education. The research protocol was approved by the Ethics Committee of Harbin Medical University (KY2017-249) and was performed in accordance with the Declaration of Helsinki. Informed consent was obtained from all the participants. Widely targeted metabolomics covering more than 1000 metabolites via liquid chromatography–tandem mass spectrometry (LC–MS) was used to compare the plasma metabolic features at baseline between 49 pairs of patients with AMI and incident heart failure within a 1-year follow-up and those without HF events.

We conducted another hospital-based nested case–control study (cohort 3) recruiting patients aged 18 years or older with STEMI between February 2019 and May 2020 from the Chinese 13·5 National Key Program for Health and Chronic Disease Management. ST-segment–elevation MI (STEMI) patients were further identified as patients with AMI and ST-segment elevation or new left bundle-branch blocks. Among the 1353 survivors at discharge, 18 patients lost to follow-up, 102 participants died without heart failure (HF), 57 patients with re-MI or stroke, and 150 patients with incident HF were identified during the 1-year follow-up after discharge and 150 controls without cardiovascular events were included via the propensity score matching method as described previously. Plasma MMA and SA were detected via liquid chromatography–tandem mass spectrometry (LC–MS). The characteristics of the participants in the three independent cohorts are presented in Tables S1–S3.

Animal studies

The animal experiments were performed according to the Guide for the Care and Use of Laboratory Animals and were approved by the Second Affiliated Hospital of Harbin Medical University Animal Care and Use Committee (number: KY201902112). All animals were given free access to drinking water and a chow diet in a facility with a 12 h light/12 h dark cycle at 23 ± 3 °C and 30–70% humidity.

Mice

Wild-type C57BL/6 mice were purchased from the Experimental Animal Center of Harbin Medical University. *Mmut* floxed mice (C57BL/6J background, $Mmut^{fl/wt}$) and α-myosin heavy chain promoter–driven heterozygous Cre (Myh6-Cre) mice were obtained from Jiangsu Cyagen Model. Cardiac-specific homozygous MMUT knockout ($Mmut^{cko}$) mice were generated by crossing MMUT flox homozygous ($Mmut^{fl/fl}$) mice with Myh6-Cre mice (C57BL/6 background). Wild-type littermates were used as controls. The age and sex of animal in each group used in the experiment are specified in the corresponding figure legends and experiment descriptions.

Littermate controls were used throughout the study. The group allocation, interventions, and data measurement for animal studies were conducted in a blinded manner and are described in the results and figure legends.

Eight-week-old mice were used to establish a cardiac I/R injury model via 45 min of coronary occlusion followed by reperfusion [19]. The mice were first anesthetized via inhalation anesthesia via 3% isoflurane (1 L/min) with an isoflurane delivery system and a heating plate was placed to maintain body temperature. A thoracotomy was subsequently performed in the third intercostal space over the left chest to expose the heart. The left anterior descending (LAD) coronary artery was ligated via a 7–0 silk suture for 45 min, and the heart was carefully returned to the chest cavity. Ischemia was identified by both ST elevation on surface electrocardiogram and the blanch heart tissues below the ligation site. After occlusion for 45 min, the slipknot was released to achieve reperfusion. Mice in the sham group were subjected to the same surgical procedure without LAD ligation. Serum and heart samples were collected for analyses at the prespecified time points after reperfusion, which are presented in the Results section and corresponding figure legends. All the mice were sacrificed at multiple time points during reperfusion, ranging from 0.5 h to 7 days, while ultrasound data were collected only at 24 h and 7 days post-reperfusion.

To specifically overexpress BNIP3 in the heart, 8-week-old $Mmut^{fl/fl}$ and $Mmut^{cko}$ mice were injected with adeno-associated virus 9 (AAV9) through the tail vein. AAV9 containing BNIP3 cDNA was driven by the cTnT promoter. The mice were intraperitoneally injected with dimethyl methylmalonate (DiMMA) (25 mg/kg/day for 7 days), dimethyl succinate (DiSA, 25 mg/kg/day for 7 days), FCCP (5 mg/kg singly), or 3-MA (20 mg/kg singly) before the IR operation.

Porcine

A total of 12 male Bama miniature pigs (25 to 30 kg, 4 months of age) were purchased from a local farm (Harbin) and fed at the experimental animal center of the Second Affiliated Hospital of Harbin Medical University. After adaptive feeding for 1–2 weeks, all animals were randomly divided into 2 groups, and either *MMUT* or empty vector of adeno-associated virus 9 (AAV9, $1.26*10^{13}$ diluted in 2 mL of phosphate-buffered saline (PBS)) was administered by direct injection into the LV wall (20 sites, 100 μL/site) 28 days before the I/R model was established. All the experiments were performed on anesthetized animals. AAV9 encoding the human *MMUT* gene was constructed and locally injected to induce cardiac overexpression. Animals were randomized to receive AAV9-*MMUT* or AAV9-GFP ($n=5$ for each group).

All pigs were established an I/R model via open chest surgery. The pigs were sedated with a cocktail of ketamine (5 mg/kg) and then diazepam (1 mg/kg) via intramuscular injection to induce anesthesia. All intravenous administrations were conducted through the ear vein at a straight segment. An intravenous infusion of propofol (5–10 mg/kg/h) was given prior to intubation. Subsequently, mechanical ventilation with a positive pressure model was used to maintain the arterial blood gases within the physiological range. The combination of an inhalatory mixture of 1–3% isoflurane dissolved in 50% air and 50% oxygen and an intravenous injection of sufentanil was used during anesthesia maintenance. After intubation, suxamethonium (20–40 μg/kg/min) was injected intravenously during surgery, and 4.3 mg/kg amiodarone dissolved in 500 mL of 0.9% sodium chloride solution was administered 30 min before coronary occlusion to prevent arrhythmia. A thoracotomy was performed through the fourth intercostal incision on the left chest wall to expose the pericardial tissues, which were then maintained under 3.0% isoflurane. After the pericardium was opened, the left anterior descending coronary artery was ligated for 60 min via a 4–0 Prolene suture distal to the second diagonal branch followed by reperfusion. The effect of coronary artery ligation was confirmed by observing myocardial cyanosis in the precardiac region and ST-segment elevation on an electrocardiogram. All the animals received intraperitoneal ampicillin for 7 days after surgery and were sacrificed 4 weeks after reperfusion via potassium chloride injection.

All animals underwent repeated echocardiography before AAV9 injection, before the I/R operation, and at 4 and 28 days after I/R injury. Two animals died of ventricular fibrillation during the I/R operation and no fatalities occurred during the 4-week after I/R. Moreover, cardiac magnetic resonance (CMR) imaging (Ingenia CX 3.0 T) was performed 4 and 28 days after I/R to evaluate the extent of myocardial injury and heart remodeling [20]. All analyses were performed by investigators blinded to the treatment arm.

Cell culture and treatment

Human AC16 and HEK 293 cell lines were obtained from the China Center for Type Culture Collection. Cell line authenticity was verified through short tandem repeat profiling, with routine mycoplasma contamination screening performed throughout the study. Cells were maintained in

DMEM (SH30022.01B, HYCLONE, USA) containing 10% fetal bovine serum (0500, ScienCell, USA) under standard conditions (37 °C, 5% CO2, humidified incubator) [21].

AC16 cells were seeded at a density of 1×10^5 cells/well in 6-well plates and incubated overnight. When the cell density reached 80%, AC16 cells were then treated with additional metabolites as follows: dimethyl methylmalonate (DiMMA, Aladdin, 609–02–9, China, 50 μM for 24 h), diethyl methylmalonate (DeMMA, Aladdin, 609–08-5, China, 25 μM for 24 h), glucose (Aladdin, G116304, China, 25 mM for 24 h), lactic acid (Absin, abs47047908, China, 0.1 mM for 24 h), pyruvic acid (Absin, abs47047907, China, 1 mM for 24 h), dimethyl succinate (DiSA, Aladdin, D103953, China, 50 μM for 24 h), homocysteine (Sigma, 44,925, USA, 20 μM for 24 h), leucine (Absin, abs47000167, China, 200 μM for 24 h), valine (Absin, abs47000153, China, 300 μM for 24 h), or isoleucine (Absin, abs47000157, China, 200 μM for 24 h), according to previous reports [22–25]. All the above reagents were dissolved in PBS and diluted in DMEM supplemented with 10% fetal bovine serum. HEK 293 cells were used for the transfection with recombinant plasmids containing mutant CREB and/or BNIP3 genes to assess their potential interaction, which was described in detail below.

MMA measurement by GC/MS

Among participants (cohort 1) in NHANES 1999–2004, MMA was measured in venous plasma and/or serum via gas chromatography–mass spectrometry (GC–MS) according to standardized protocols. The accordance of MMA concentrations in the pairs of serum and plasma has been validated in a previous study [26]. All blood specimens were collected at mobile examination centers and analyzed at the prespecified central laboratory. The detection protocol has been described previously. High-performance GC/MS (Model 6890 GC system and Model 5973 mass selective detector, Hewlett-Packard, San Fernando, CA) with DB-5MS capillary GC column (0.25 μm; J&W Scientific, Folsom, CA) was used for chromatographic separation. Briefly, 275 μL of each sample was combined with an internal standard (isotope-labeled methyl-d3-malonic acid) and underwent derivatization using cyclohexanol, yielding the corresponding dicyclohexyl ester. Following derivatization, analytes were separated via gas chromatography (15 min per run) and detected using a mass selective detector operating in selected ion monitoring mode. MMA concentrations were determined by comparing peak area ratios between MMA and its deuterated internal standard (d3MMA). The assay demonstrated linearity across the 50–2000 nmol/L range. Samples exceeding 400 nmol/L underwent repeat analysis. Method validation revealed a total coefficient of variation of 4–10% and an average recovery of 96.0 ± 1.9%.

Widely targeted metabolomics

Widely targeted metabolomics was performed in peripheral vein blood samples in cohort 2. Plasma samples were collected after centrifugation at 1500 × g. Widely targeted metabolomic profiling was performed by Wuhan MetWare Biotechnology (https://sciex.com/). Specific procedures for hydrophilic and hydrophobic compound extraction, chromatographic separation, and mass spectrometric detection were carried out.

Hydrophilic metabolites

The plasma stored at − 80 °C was thawed in ice water and vortexed for 10 s. Thirty microliters of sample and 180 μL of extraction solution (ACN:methanol = 1:4, V/V) containing internal standards were mixed for 3 min and then centrifuged at 12,000 rpm for 10 min (4 °C). Then, 120 μL aliquots of the supernatant were transferred for analysis via an LC–ESI–MS/MS system (UPLC, ExionLC AD, https://sciex.com.cn/; MS, QTRAP® System, https://sciex.com/). Chromatographic separation was achieved using a Waters ACQUITY UPLC HSS T3 C18 column (1.8 μm, 2.1 mm × 100 mm) maintained at 40 °C with a flow rate of 0.4 mL/min and 2 μL injection volume. The mobile phase consisted of water and acetonitrile (both containing 0.1% formic acid) with the following gradient elution program (v/v): 95:5 (0 min), 10:90 (11.0 min), 10:90 (12.0 min), 95:5 (12.1 min), and 95:5 (14.0 min).

Mass spectrometric detection employed a triple quadrupole-linear ion trap instrument (QTRAP® LC–MS/MS System) fitted with an ESI Turbo Ion-Spray interface, controlled via Analyst 1.6.3 software (Sciex). Data acquisition utilized both LIT and triple quadrupole scanning modes in positive and negative ionization. ESI source parameters included temperature, 500 °C; ion spray voltage, 5500 V (positive) and − 4500 V (negative); and gas settings for GSI, GSII, and CUR at 55, 60, and 25.0 psi, respectively, with CAD maintained at high pressure. Calibration was conducted using polypropylene glycol solutions at 10 μmol/L (QQQ mode) and 100 μmol/L (LIT mode). Multiple reaction monitoring (MRM) transitions were optimized for each chromatographic window based on metabolite elution profiles.

Hydrophobic metabolites

Fifty microliters of plasma and 1 mL of extraction solvent (MTBE:MeOH = 3:1, v/v) containing an internal standard mixture were mixed. After the mixture was allowed to warm for 15 min, 200 μL of water was added. The

mixture was vortexed for 1 min and centrifuged at 12,000 rpm for 10 min. Two hundred microliters of the upper organic layer was collected and evaporated via a vacuum concentrator. The dry extract was dissolved in 200 μL of reconstituted solution (ACN:IPA = 1:1, v/v) for LC–MS/MS analysis.

Sample extracts were analyzed using an LC–ESI–MS/MS platform (UPLC: ExionLC AD, https://sciex.com.cn/; MS: QTRAP® System, https://sciex.com/). Chromatographic separation utilized a Thermo Accucore™ C30 column (2.6 μm, 2.1 mm × 100 mm) at 45 °C with a 0.35 mL/min flow rate and 2 μL injection volume. The binary mobile phase comprised (A) acetonitrile/water (60/40, v/v) and (B) acetonitrile/isopropanol (10/90, v/v), both supplemented with 0.1% formic acid and 10 mmol/L ammonium formate. Gradient elution proceeded as follows (A:B, v/v): 80:20 (0 min), 70:30 (2.0 min), 40:60 (4 min), 15:85 (9 min), 10:90 (14 min), 5:95 (15.5–17.3 min), returning to 80:20 (17.3–20 min).

Mass spectrometric analysis employed a triple quadrupole-linear ion trap instrument (QTRAP® LC–MS/MS System) with ESI Turbo Ion-Spray interface, operated via Analyst 1.6.3 software (Sciex) in dual ionization modes. The turbo spray source was configured with temperature at 500 °C; spray voltage at 5500 V (positive) and −4500 V (negative); GS1, GS2, and CUR pressures at 45, 55, and 35 psi, respectively; and CAD set to medium. System calibration utilized polypropylene glycol at 10 μmol/L (QQQ mode) and 100 μmol/L (LIT mode). Multiple reaction monitoring was conducted in QQQ mode with nitrogen collision gas at 5 psi, with optimized declustering potential (DP) and collision energy (CE) parameters for individual transitions. MRM acquisition windows were tailored to metabolite retention times throughout each chromatographic segment.

Targeted detection of MMA and SA via LC–MS/MS

Among participants in cohort 3, stable-isotope-dilution LC–MS/MS was used for the quantification of methylmalonic acid (MMA) via established methods for quantifying analytes in biological matrices with optimized accuracy, precision, and minimal matrix effects, as described previously. Briefly, ice-cold 20% acetonitrile/methanol containing an internal standard (D3-methylmalonic acid, D3-MMA) was added to the plasma samples, followed by vortexing and centrifugation. The supernatant was lyophilized in a centrifugal vacuum evaporator at 30 °C. The sample was reconstituted in 25 μL of 50% (vol/vol) H_2O/methanol, followed by vortexing and centrifugation. The clear supernatant was transferred to glass vials with micro inserts, and LC–MS/MS analysis was performed with an UltiMate 3000 UHPLC system (Thermo Fisher) coupled to a TSQ Quantis triple quadruple mass spectrometer (Thermo Fisher). For chromatographic separation, an ACQUITY HSS T3 column (i.d. 2.1 × 100 mm, 1.8 μm) (Waters) was used. Electrospray ionization in negative mode with selected reaction monitoring (SRM) was used with the following transitions: m/z 117.00 → 55.071 and 117.00 → 73.00 for MMA and m/z 120.05 → 58.125 and 120.05 → 76.071 for D3-MMA. The data analysis software TraceFinder (Thermo Fisher) was used. The total coefficient of variation (CV) was 3.5–6.8% at different concentration ranges, the average recovery rate was 96.3 ± 2.2% for MMA measurement, and the corresponding indicators for SA detection were 4.2–8.7% and 95.0 ± 3.1%, respectively.

Vitamin B12 measurement

Serum vitamin B12 levels were measured via the Bio-Rad Laboratories Quantaphase II radioimmunoassay in NHANES 1999–2004 [27]. The coefficient of variation of the serum vitamin B12 concentration was less than 5%.

High-sensitivity cardiac troponin T/I measurement

Frozen serum samples collected during the NHANES 1999–2004 cycles were subjected to testing for hs-cTnT and hs-cTnI at the University of Maryland School of Medicine in Baltimore, MD, between 2018 and 2020 [26]. Most of the stored specimens (93%) had not undergone freeze–thaw cycles. Hs-cTnT levels were measured via a Roche Cobas e601 (Roche Diagnostics Corporation, Indianapolis, IN). The limit of detection (LOD) for this assay reached 3 ng/L, and total coefficients of variation (CVs) were 2.0–3.1% at different concentration ranges. High-sensitivity troponin I (Abbott) in each blood sample was measured via 3 independent assays: Abbott (ARCHITECT i2000SR), Siemens (Centaur XPT), and Ortho (Vitros 3600). For the Abbott, Siemens, and Ortho assays, the LODs were 1.7 ng/L, 1.6 ng/L, and 0.39 ng/L, respectively; the CVs across different concentration ranges for the three hs-TnI assays were 3.5–6.7%, 2.6–3.8%, and 2.8–4.2%, respectively.

Proteomics and acetylproteomics

PTMBiolabs (Hangzhou, China) conducted all proteomic and acetylproteomic analyses. Cell samples underwent lysis and protein extraction using buffer containing 8 M urea, 1% protease inhibitor cocktail, 3 μM TSA, and 50 mM NAM for acetylation analysis. Following protein concentration determination, trypsin digestion was performed at 1:50 and 1:100 trypsin-to-protein mass ratios. Resulting peptides underwent TMT labeling and HPLC-based fractionation. Pan-antibody enrichment was achieved by incubating tryptic peptides with pre-washed antibody beads, followed by high-resolution LC–MS/MS analysis. MaxQuant software (v. 1.5.2.8)

processed the acquired LC–MS/MS data. Tandem mass spectra searched the human UniProt database combined with its reverse decoy counterpart. To eliminate protein expression effects on modification abundance, quantitative normalization was applied prior to downstream bioinformatics analyses. Differential modification sites met the following criteria: fold change ≥ 1.3 and *t*-test *P* value < 0.05.

Oxylipins

Previous studies validated the experimental protocols employed [28]. Frozen heart tissue (− 80 °C) was thawed on ice, and 20 mg samples underwent protein precipitation using 0.2 mL methanol containing internal standard. To prevent oxidative degradation during extraction, butylated hydroxytoluene (0.005%) was incorporated. Eicosanoids from the resulting supernatants underwent purification using Poly-Sery MAX SPE columns (ANPEL). Extracted compounds were characterized by LC–ESI–MS/MS (UPLC: ExionLC AD; MS: QTRAP® 6500 + System) with a Waters ACQUITY UPLC HSS T3 C18 column (100 mm × 2.1 mm i.d. 1.8 μm). The 10-min binary gradient utilized mobile phases comprising (A) water/acetic acid (0.04%) and (B) acetonitrile/acetic acid (0.04%). Oxylipin metabolic profiles were obtained through scheduled multiple reaction monitoring, with absolute quantification achieved using eicosanoid-specific calibration curves.

CMR assessment for the porcine model

CMR assessment was conducted in a porcine model at 3 (early phase) and 28 (late remodeling phase) days after I/R injury via a 3.0T CMR system (Ingenia CX, Philips) [29, 30]. The acquisition of CMR data was performed by a CMR-specialized technician who was blinded to the intervention. The following dedicated CMR sequences were acquired: a balanced steady-state free-precession imaging sequence to assess wall motion (WM) and heart function, a T2-weighted short-tau inversion recovery (T2-STIR) sequence to assess myocardial edema, and a late gadolinium enhancement (LGE) sequence to assess the amount and extent of myocardial infarction.

For CMR studies, animal anesthetization was induced by intramuscular injection of a cocktail composed of ketamine, xylazine, and atropine and maintained by continuous intravenous infusion of propofol. When pigs were positioned in a head-first supine position with a flexible phased-array surface coil over the chest, scout images (T1-TFE sequence) were acquired to localize the axes of the heart and define the view field of the whole heart. Steady-state free-precession cine imaging was performed in both the horizontal and vertical long axes. Short-axis images covering the whole left ventricle (TR 3.6 ms, TE 1.6 ms, flip angle 45°, field of view (FOV) 250 × 250 mm, SENSE factor 3, voxel size 1 × 1 × 5 mm, no gap, number of averages 3, bandwidth 1286 Hz, 12 lines per segment) were obtained for the quantification of LV motion and function. Thereafter, the T2-STIR sequence was obtained to assess myocardial edema. Gadolinium was injected into the auricular vein for an enhancement scan to assess the amount and extent of myocardial necrosis (day 3) or scarring (day 28). Afterward, late gadolinium enhancement (LGE) was performed 10 min after intravenous injection of a gadolinium-based contrast agent (Gd-GTPA, Magnevist, 0.2 mmol/kg). The scanning parameters for the phase-sensitive inversion recovery (PSIR) sequence were set as follows: TR, 6.1 ms; TE, 3.0 ms; FOV, 300 × 300 mm2; voxels, 1.8 × 1.68 × 8.0 mm; flip angle, 25°; and slice thickness, 8 mm.

LV epicardial and endocardial borders were traced in each cine image of the cardiac phases representing the end-diastole and end-systole to obtain the left ventricular end-diastolic volume (LVEDV), left ventricular end-systolic volume (LVESV), left ventricular ejection fraction (LVEF), and LV mass. For assessment of the area at risk, endocardial and epicardial borders were manually traced in each contiguous short-axis view. The area of myocardial edema was defined as the extent of the LV hyperintense area on T2-STIR images. An edema area was regarded as hyperintense when the signal intensity was greater than 3 standard deviations of the signal intensity in remote, normal myocardium. The size of the infarction (day 3) was quantified from the extent of myocardial enhancement in the LGE CMR sequence. Myocardial infarction was defined as a myocardium with a signal intensity greater than 3 standard deviations of that in remote, normal myocardium. The LV infarct size is expressed as a percentage of the area of myocardial edema. All CMR images were measured by 2 independent CMR-trained radiologists in a blinded fashion via commercially available software (cvi42, Circle Cardiovascular Imaging). The intra- and interobserver variabilities obtained for the CMR indicators were 4.4 ± 2.3% and 9.5 ± 6.8%, respectively.

Echocardiography assessment for both animal models

Anesthetized mice (3.0% isoflurane with O2 at 1.0 L/min) underwent two-dimensional echocardiographic assessment using a Vevo 3100LT system equipped with an MS400 transducer. Parasternal short-axis images were acquired and archived for subsequent offline evaluation by two blinded observers using Vevo 3100 software. Cardiac functional parameters derived from the analysis included ejection fraction (EF), fractional shortening (FS), end-systolic and end-diastolic internal diameters (LVIDs, LVIDd), anterior wall dimensions in systole and

diastole (LVAWs, LVAWd), and posterior wall thickness measurements at end-systole and end-diastole (LVPWs, LVPWd) [31].

For the pig model, echocardiography was performed before AAV9 injection, before the I/R operation, and at 4 days and 4 weeks post-MI. Animal anesthetization was induced by intramuscular injection of a cocktail (ketamine, xylazine, and atropine) and maintained by continuous intravenous infusion of propofol (10 mg/kg/h). Transthoracic 2D echocardiography was performed via an EPIQ5 system with an S5 transducer (1–5 MHz frequency, Philips Medical Systems, USA). Images were acquired and measured by staff who were blinded to the experimental treatments.

Infarct size measurements

Infarct size and area at risk (AAR) following I/R injury were assessed using 2,3,5-triphenyl tetrazolium chloride (TTC)-Evans blue double staining [32]. Twenty-four hours post-reperfusion, mice were euthanized, and the LAD was reoccluded at the original ligation site. Cardiac tissue was perfused with 1 mL of 1% Evans blue (Biofroxx, EZ5679B136, Germany), excised, and rinsed with cold PBS. After 30-min freezing (−80 °C), hearts underwent serial sectioning (1–2 mm thickness) from the ligation point toward the apex. Sections were stained with 2.0% TTC (Solarbio, G3005, China) for 15 min at 37 °C, then immersed in ice-cold sterile saline to halt the reaction, followed by 5-min fixation in 4% neutral-buffered formaldehyde. Photographic documentation of each section enabled computerized planimetric analysis (ImageJ v1.51) to quantify the infarcted region (pale) and AAR (pale plus pink regions). Infarct size was expressed as the ratio of infarcted tissue to AAR, with all measurements performed by blinded investigators.

Pathological analyses of the pig I/R model were conducted 28 days after the I/R procedure. The pigs were anesthetized with ketamine (5 mg/kg) and then diazepam (1 mg/kg) and sacrificed with 10% KCl. The heart was removed, washed in chilled saline, and then chilled with phosphate-buffered saline. Hearts were then weighed and sectioned into 2 cm slices from the apex to the base for histological analysis. Each slice was photographed, and the scar area (pale area) was measured via computerized planimetry (ImageJ v1.51). The infarct size was calculated as the infarct area divided by the LV, and all the data were analyzed in a blinded manner.

Pathological staining

Histological analysis of heart slices from mice or pigs was performed at different time points. Heart tissues were fixed with 4% paraformaldehyde at room temperature for 72 h, paraffin-embedded, and sliced into 4 μm thick sections. Sections were stained with hematoxylin and eosin (H&E) (Right Tech, China) or Masson's trichrome stain as previously described [31].

Immunofluorescence

Mitophagy was visualized through colocalization analysis of the mitochondrial marker TOM20 with LC3. Immunofluorescence sections were air-dried for 10 min at room temperature (RT) before undergoing cold acetone fixation (−20 °C, 10 min). Following three distilled water rinses, sections underwent permeabilization with 0.3% Triton-X 100 (37 °C, 30 min) and overnight primary antibody exposure at 4 °C. The next day, after RT equilibration (10 min), secondary antibody incubation proceeded for 1 h at RT. Nuclear counterstaining utilized DAPI (0.5 g/L, 10 min), and fluorescent imaging was performed using a Zeiss LSM 700 confocal laser scanning microscope.

Transmission electron microscopy (TEM)

Heart tissue was fixed with 2.5% glutaraldehyde, 2.5% polyvidone 25, and 0.1 M sodium cacodylate (pH 7.4). After being washed with 0.1 M sodium cacodylate buffer (pH 7.4), the samples were fixed in the same buffer containing 2% osmium tetroxide and 1.5% potassium ferrocyanide for 1 h. The samples were rinsed once in water, stained en bloc with uranyl acetate, dehydrated via an ascending ethanol series, and embedded in Durcupan ACM-based resin. Ultrathin sections were cut via a Reichert Ultracut S ultramicrotome (Science Service, Munich, Germany), and lead citrate was used for contrast. Images were captured via an EM 10 CR electron microscope (H-7650; Hitachi, Tokyo, Japan) and analyzed by an independent, blinded investigator.

Assessment of apoptosis

Cardiac apoptosis was quantified using terminal deoxynucleotidyl transferase-mediated dUTP nick end labeling (TUNEL; Elabscience Biotechnology Co., Ltd., China, E-CK-A321) according to previously published protocols [28]. The apoptosis index represented the ratio of TUNEL-positive to total nuclei across five randomly selected fields per sample.

Mitochondrial membrane potential

Mitochondrial membrane potential was evaluated using a JC-1 fluorescent probe kit (Beyotime, China, C2005). This voltage-sensitive dye exhibits potential-dependent fluorescence patterns: forming red-fluorescent aggregates within polarized mitochondria and green-fluorescent monomers upon membrane depolarization. AC16 cells received JC-1 solution and underwent 20-min incubation at 37 °C under light-protected conditions. Following

triple PBS washing, specimens were visualized using a Leica fluorescence microscope (Germany). Fluorescence intensities of both monomeric and aggregated forms were quantified from five randomly acquired images per sample.

Reactive oxygen species assessment

Reactive oxygen species (ROS) generation in fresh cardiac tissue was detected using DHE and MitoSOX fluorescent probes. Cryosections underwent 10-min PBS pretreatment before exposure to DHE (10 μmol/L, Beyotime, China, S0063) for 30 min at 37 °C under light-protected conditions. Following triple PBS rinsing, fluorescence signals were captured using a Leica microscope (Germany).

Oxygen consumption rate measurement

The oxygen consumption rate (OCR) was assessed using a Seahorse Bioscience XF-96 Extracellular Flux Analyzer (Agilent Technologies) in conjunction with a Mito Stress Test Kit (Agilent, 103,015–100, USA). Prior to the assay, the XFe96 Sensor Cartridge was hydrated by adding 200 μL of sterile calibrant solution to each well of the utility plate, followed by overnight incubation at 37 °C in a CO2-free environment. AC16 cells were plated onto XFe96 cell culture microplates (Agilent, 101,085–004, USA) at 1×10^4 cells/well and cultured overnight to ensure proper attachment. Before measurement, the growth medium was exchanged with Seahorse XF DMEM (Agilent, 103,575–100, USA) supplemented with glucose (10 mM), glutamine (2 mM), and pyruvate (1 mM), and cells were equilibrated for 1 h at 37 °C without CO2. Real-time OCR measurements were then performed following baseline readings, with sequential administration of mitochondrial modulators according to the manufacturer's protocol: oligomycin (10 μM, 20 μL) via port A, FCCP (10 μM, 22 μL) via port B, and a rotenone/antimycin A mixture (5 μM, 25 μL) via port C.

Immunoprecipitation

To detect CREB acetylation, we performed immunoprecipitation. AC16 cells were lysed in IP buffer (Beyotime, P0013, China) and vortexed for 15 s every 5 min for 30 min at 4 °C. The lysates were incubated with 10 μg of anti-acetylate lysine antibody (Cell Signaling Technology, 9441 s) overnight at 4 °C on a rotating platform. The immune complexes were bound to protein A/G magnetic beads and collected via a magnetic stand. After being washed 3 times with IP buffer, the bound proteins were heated to 95 °C for 10 min in sodium dodecyl sulfate (SDS) loading buffer. Immunoblotting analysis was performed with an anti-CREB antibody. The supernatants were used for western blotting.

Chromatin immunoprecipitation (ChIP) assay

Chromatin immunoprecipitation (ChIP) assays were conducted using a commercial kit (Wanleibio, WLA106a) following the provided protocol. Briefly, AC16 cells were subjected to chemical cross-linking with 1% formaldehyde for 10 min at room temperature, after which the reaction was terminated by adding 0.125 M glycine [33]. Following cell lysis, chromatin was sheared to generate DNA fragments ranging from 150 to 900 bp in length. Immunoprecipitation was subsequently carried out using a ChIP-grade anti-CREB antibody (CST, 9197), with IgG from the kit serving as a negative control. After purification, the precipitated DNA was subjected to PCR amplification using two primer sets specifically designed to target distinct CREB binding regions within the BNIP3 promoter. The resulting PCR products were visualized by agarose gel electrophoresis. The primer pairs utilized were as follows: BNIP3-1 (forward: ACCGCCTGAGGT GAGCCG; reverse: GGCACTGGCTACCACGGAGAC) and BNIP3-2 (forward: CCGTCTTTCCATCCTGCT AGTG; reverse: AGGAAGAAGCGGAGGCTCG).

Gene mutagenesis and dual luciferase reporter gene assays

AC16 cells grown in 24-well plates were cotransfected with a firefly reporter vector or Renilla reporter vector together with an empty plasmid or plasmids encoding a constitutively wild-type (−1490/+117 bp) or BNIP3 mutant (deleting the proximal promoter region of BNIP3 at positions between −498 and −487 bp and between −300 and −289 bp, respectively). Because lysine (K) residues 309 and 325 are potential binding sites for hyperacetylation of CREB, we mutated both the K residues in CREB to mimic a protein deacetylation state and the glutamine (Q) to mimic a protein hyperacetylation state with a flag label. These plasmids were constructed by Cyagen Biosciences (Guangzhou, China). Lipo3000 (L3000008, Invitrogen Thermo Fisher, USA) was used for transfection, and the cells were solubilized in lysis buffer (MF648-01, Mei5bio, China) after 48 h. AC16 cells were transfected with luciferase-expressing vectors driven by the human BNIP3 promoter for 48 h. Luciferase activity was measured with a microplate reader (Tecan Infinite 200 Pro). Firefly luciferase activity was normalized to Renilla luciferase activity.

Construction and transfection of recombinant plasmids

The full-length sequences of Sirt1, Sirt2, MMUT, and CREB were obtained from human peritoneal macrophage cDNA and then cloned and inserted into the pcDNA3.1 vector, which contains different tags. Deleted, truncated, and point mutants were generated via PCR-based amplification, and the

construct encoding the wild-type protein was used as the template. All the constructs were confirmed via DNA sequencing. The primers used are listed in Table S9. Point mutations in the reconstructed CREB gene were then introduced via the Fast Mutagenesis Kit (TransGene, Beijing, China). The full-length sequences of CREB-WT, CREB-K309R, CREB-K325R, CREB-K309/325R, CREB-K309Q, and CREB-K325Q were cloned and inserted into the flag vector. In silico analysis identified two potential CREB-responsive domains within the proximal region of BNIP3 promoter at positions between − 498 and − 487 bp and between − 300 and − 289 bp. To determine the functional sites in the BNIP3 promoter, each of the segment in BNIP3 promoter was deleted to construct plasmids containing mutated BNIP3 promoters (Fig. 7L). After DNA sequencing confirmation, recombinant plasmids were transiently transfected into HEK 293 cells within Opti-MEM medium and Lipofectamine™ 3000 (Thermo). Dual luciferase reporter gene assays were performed via cotransfection with luciferase-expressing vectors driven by the BNIP3 promoter.

Enzyme-linked immunosorbent assay (ELISA) kits and activity assay

At the experimental endpoints, blood samples were collected and left undisturbed at room temperature for 30 min. Serum was then separated by centrifugation (3000 rpm, 15 min, 4 °C) and the supernatant was harvested for subsequent analysis. For cellular experiments, AC16 cells were pelleted by centrifugation following the designated treatments. The levels of CK-MB (creatine kinase isoenzyme-MB; Elabscience, E-E-M0355c, China or CUSABIO, CSB-EQ027653PI, China), cTn-I (CUSABIO, CSB-E11187p, China), LDH (lactate dehydrogenase; Elabscience, E-BC-K046-M, China), and ATP (Elabscience, E-BC-K157-M, China) were determined in mouse serum, pig serum, and AC16 cell lysates from various experimental groups using corresponding ELISA kits or enzymatic activity assay kits in accordance with the manufacturers' instructions. SIRT activity was determined with a Universal SIRT Activity Assay Kit (ab156915, Abcam) according to previous methods [34]. The SIRT1 protein was immunoprecipitated from heart tissue lysates via an anti-Sirt1 antibody. After washing three times, the SIRT1 proteins were incubated with the substrate and assay buffer for 2 h at 37 °C. The absorbance at 450 nm was recorded via a microplate reader (Infinite F500, Tecan Group, Ltd.). The SIRT activity was calculated according to the manufacturer's protocol.

Western blotting

Total protein was isolated from AC16 cells or cardiac tissues using RIPA lysis buffer supplemented with protease and phosphatase inhibitors. Subcellular fractionation of mitochondrial and cytosolic components was accomplished using a commercial kit (EnoGene, E1WP1031, China). Protein concentrations were quantified with a bicinchoninic acid assay (Beyotime, P0012, China). Equal amounts of protein (30 μg per lane) were resolved by 10% or 12.5% SDS-PAGE and subsequently electrotransferred onto 0.22 μm PVDF membranes (Beyotime, FFP70, China). Membranes were blocked with 5% nonfat dry milk prepared in Tris-buffered saline containing 0.05% Tween 20 for 2 h at room temperature, followed by overnight incubation with the appropriate primary antibodies at 4 °C. After washing, membranes were probed with HRP-conjugated secondary antibodies (1:8000 dilution) for 1 h at room temperature. Immunoreactive bands were detected using an ECL detection system (Meilunbio, MA0186-1-Jul-14H, China) and visualized with a ChemiDoc™ MP Imaging System (Tanon, China). Densitometric analysis was performed using Bio-Rad Quantity One software (Tanon, China), with band intensities normalized to GAPDH or VDAC1 as loading controls. For posttranslational modification (PTM) analysis, total protein quantification was conducted using Coomassie brilliant blue staining (Beyotime, P0003S, China). Primary and secondary antibodies were diluted in TBST (Tris-buffered saline with 0.1% Tween 20) containing 5% skim milk powder.

Real-time quantitative PCR (RT–qPCR)

RNAs were harvested via TRIzol reagent (HaiGene, China, B0201) and reverse-transcribed to cDNA via the RT Easy II First Strand cDNA Synthesis Kit (Roche, Switzerland, 04379012001). The target genes were amplified via a real-time PCR system (SYBR Green I, MCE, China; HY-K0501). Gene expression was normalized to the β-actin level and calculated via the − ΔΔCT method. The primers used are presented in Table S8, and the gene expression values were normalized against those of β-actin.

Statistical analysis

All quantitative data are presented as the means ± standard deviations (SDs) unless otherwise noted. R (version 4.2) and GraphPad Prism (version 10.0) were used for statistical analysis and visualization. Comparisons were conducted using Student's *t*-test for two groups and one/two-way ANOVA with Tukey's post hoc test for multiple groups. Principal component analysis (PCA) and partial least squares-discriminant analysis (PLS-DA) were

used to assess the different features in the omics data. All ChIP-seq data from previous studies are publicly available in the Gene Expression Omnibus (www.ncbi.nlm.nih.gov/geo) under the accession numbers GSE99895 and GSE73769. ChIP-seq data were generated with an integrative genomics viewer (http://software.broadinstitute.org/software/igv/). A difference was considered statistically significant if the *P* value was less than 0.05.

Results

MMA elevation predicts myocardial injury and incident HF post-reperfusion in humans that outmatches its isomer succinate

Although our previous studies found an association between MMA and cardiovascular mortality risk [8, 13], the specific mechanism involved remained unclear. We next investigated the association between MMA and subclinical myocardial vulnerability. Compared with those with MMA < 120 nmol/L, individuals with MMA elevation (≥ 250 nmol/L) had a nearly tenfold increase in the prevalence of subclinical myocardial injury (hs-cTnT > 14 ng/L) among 11,410 CVD-free adults (Fig. 1A–C and Additional file 1: Table S1). This association was reproducible for elevated hs-cTnI levels assessed by three independent assays (Fig. 1C). Although vitamin B12 functions as a coenzyme of methylmalonate metabolism [27], B12 deficiency (< 150 pmol/L) was not related to subclinical myocardial injury (Fig. 1B). These results suggest a link between MMA elevation and myocardial vulnerability.

Given that HF is the primary challenge post-I/R, we further conducted widely targeted metabolomics on 49 pairs of inpatients with AMI with or without incident HF during a 1-year follow-up using plasma collected after pPCI (Fig. 1D and Additional file 1: Table S2). The metabolic profiles differed significantly between the HF and non-HF groups according to PCA and PLS-DA (Fig. 1E). Among the 244 different metabolites (absolute fold change > 1.2 and *P* value < 0.05), the primary enrichment was involved in branched-chain amino acid metabolism and mitochondrial energy metabolism (Fig. 1F). Consistent with previous reports [35], the isomers MMA and succinate were difficult to separate under general liquid chromatography conditions. Nonetheless, plasma isoleucine and valine, precursors of MMA, were higher in AMI patients with incident HF than in those without events (Fig. 1G and H).

We further developed rapid and efficient LC–MS/MS protocols to determine circulating MMA and succinate after pPCI among another 150 pairs of AMI patients with or without incident HF during the 12-month follow-up period (Fig. 1I and Additional file 1: Table S3). Although both MMA and succinate were higher in HF group than those without HF, only MMA was significantly associated with HF risk post-infarction in multivariable-adjusted analysis (Fig. 1I–K). Compared with succinate, serum MMA had a superior predictive performance for HF risk (ROC_{AUC} 0.754 versus 0.640) as well as stronger correlations with myocardial biomarkers, such as CK, CK-MB, and cTnI (Fig. 1L and Additional file 1: Fig. S1A). These findings indicated that individuals with elevated MMA levels were more prone to myocardial injury and subsequent HF risk than succinate elevation in humans.

Distinct changes in cardiac MMA and succinate in mice post-ischemia/reperfusion

Consistent with observations in humans, MMA levels in heart tissues of mice doubled after 24 h of I/R, whereas alterations in cardiac succinate levels were minor (Fig. 2A), although both metabolites in serum were elevated post-reperfusion (Fig. 2B). We further depicted the temporal trend in both isomers after reperfusion of 2 weeks. Compared with the baseline levels, MMA level was greater for up to 2 weeks post-I/R, whereas cardiac succinate rapidly decreased to baseline levels after an initial increase during the reperfusion period (Fig. 2C and D). This may be related to the recovery of succinate dehydrogenase activity after reperfusion. Given that MMUT mutation is the primary cause of methylmalonic acidemia with no response to vitamin B12 [36], we further assessed the cardiac protein expression of MMUT in mice subjected to LAD ligation for 45 min followed by reperfusion for 24 h. MMUT expression was significantly lower in the border zone of the I/R heart than in that of the sham control (Fig. 2E). Furthermore, the increase in serum MMA concentration post-reperfusion originated from other organs was excluded (Fig. 2F). Specifically, immunofluorescence staining showed that MMUT primarily colocalized with the myocardium marker troponin I, whereas its colocalization with the endothelial cell marker CD31 and the fibroblast marker α-SMA was less pronounced (Fig. 2G). Among over 60 types of tissues and cells from WT mice, cardiac *Mmut* expression ranked fourth, surpassed only that in the kidney, brown fat, and liver (Fig. 2H), suggesting that the heart exhibited an active MMA metabolic process, rendering it susceptible to MMA accumulation when this process is blocked under pathological conditions. Overall, these findings suggest that sustained MMA elevation in heart tissues is observed post-I/R compared with the transient increase in its isomer succinate.

Methylmalonate aggravated myocardial ischemia/reperfusion injury

We next investigated the impacts of MMA and succinate administration on myocardial vulnerability post-I/R.

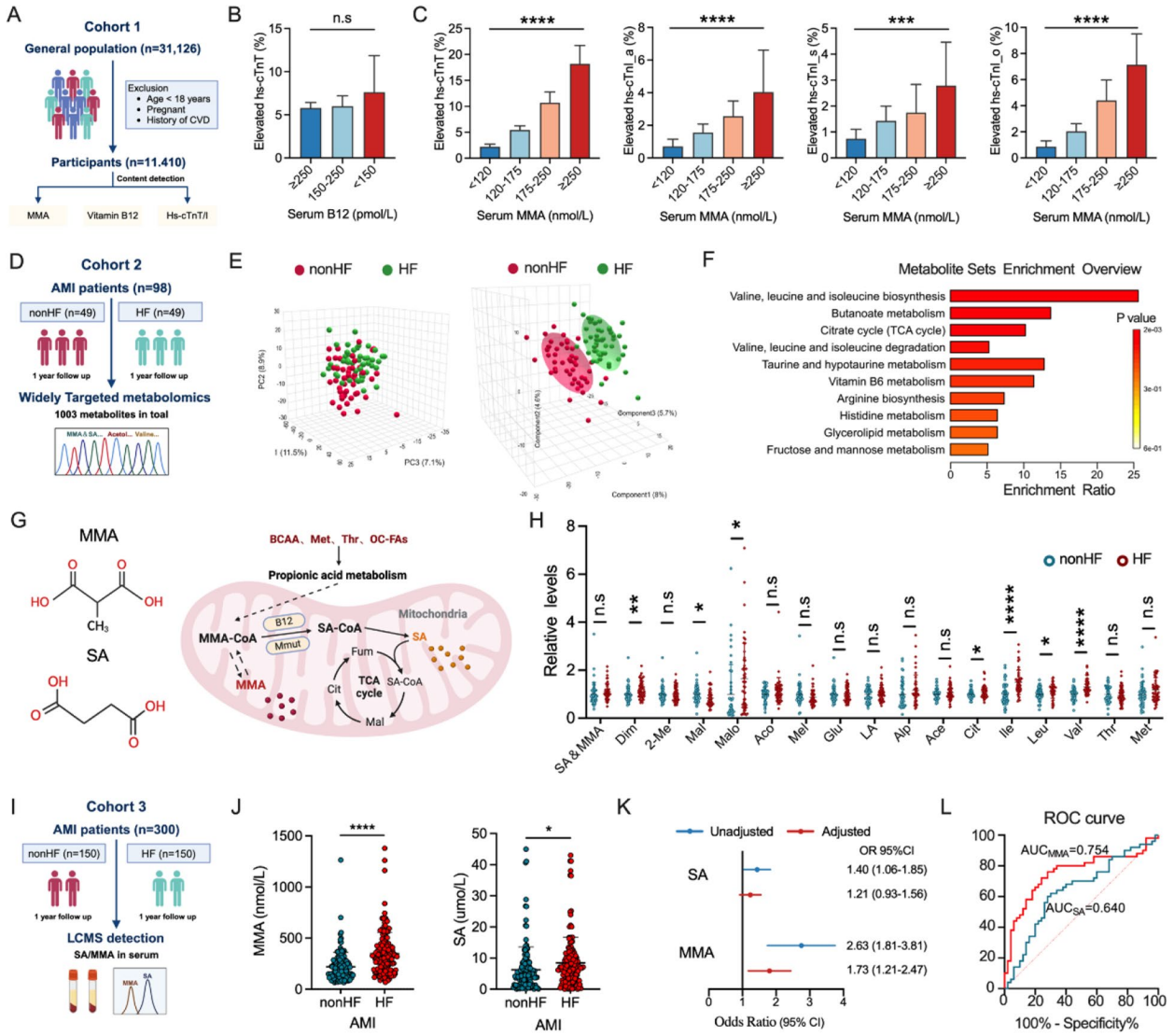


Fig. 1 MMA predicts myocardial injury and incident heart failure compared with its coenzyme vitamin B12 and the isomer succinate. **A** Flow of the study (cohort 1), including 11,410 general adults aged ≥ 20 years after excluding pregnant women or those with a history of CVD. **B** The weighted prevalence and 95% CI of elevated hs-cTnT across serum vitamin B12 levels. **C** The weighted prevalence and 95% CI of elevated hs-cTnT (Roche assay) and hs-cTnI (3 independent Abbott, Siemens, and Ortho assays) across serum MMA levels. **D** Flow of the study (cohort 2), including 49 pairs of patients with AMI and incident heart failure within a 1-year follow-up and those without HF events to conduct widely targeted metabolomics in baseline plasma after pPCI. **E** Principal component analysis (PCA) and partial least squares-discriminant analysis (PLS-DA). **F** Kyoto Encyclopedia of Genes and Genomes pathway enrichment analysis of differentially abundant metabolites in both groups. **G** Molecular structure and schematic overview of MMA- and succinate (SA)-related metabolic processes. **H** Relative levels of MMA/SA-related metabolites. **I** Flow of the study (cohort 3), including 300 age- and sex-matched patients with or without incident HF during 1-year follow-up post-MI for targeted detection of baseline MMA and SA levels after pPCI. **J** Distribution of MMA and SA according to follow-up outcomes. **K** Unadjusted and multivariable-adjusted OR (95% CI) of the associations of MMA or SA with incident HF. **L** Receiver operating characteristic curves of MMA and SA for the prediction of HF risk. Statistics: *P* values for trend were determined by weighted generalized linear regression (**B**, **C**); *P* values were calculated using Student's *t*-test (**H**, **J**). Data are presented as weighted prevalence and 95% CI (**B**, **C**) and the mean ± SD (**H**, **J**); *$P < 0.05$; **$P < 0.01$; ***$P < 0.001$; ****$P < 0.0001$; n.s., not significant

Exogenous MMA causes alterations in cellular phenotypes dependent on high concentrations [21, 25], due to lower cellular permeability than serum MMA, which is identified as a lipidic structure [25]. Therefore, mice were intraperitoneally injected with more cell-permeable dimethyl methylmalonate (DiMMA) or dimethyl succinate (DiSA). Compared with vehicle treatment, DiMMA injection aggravated cardiac systolic dysfunction and the

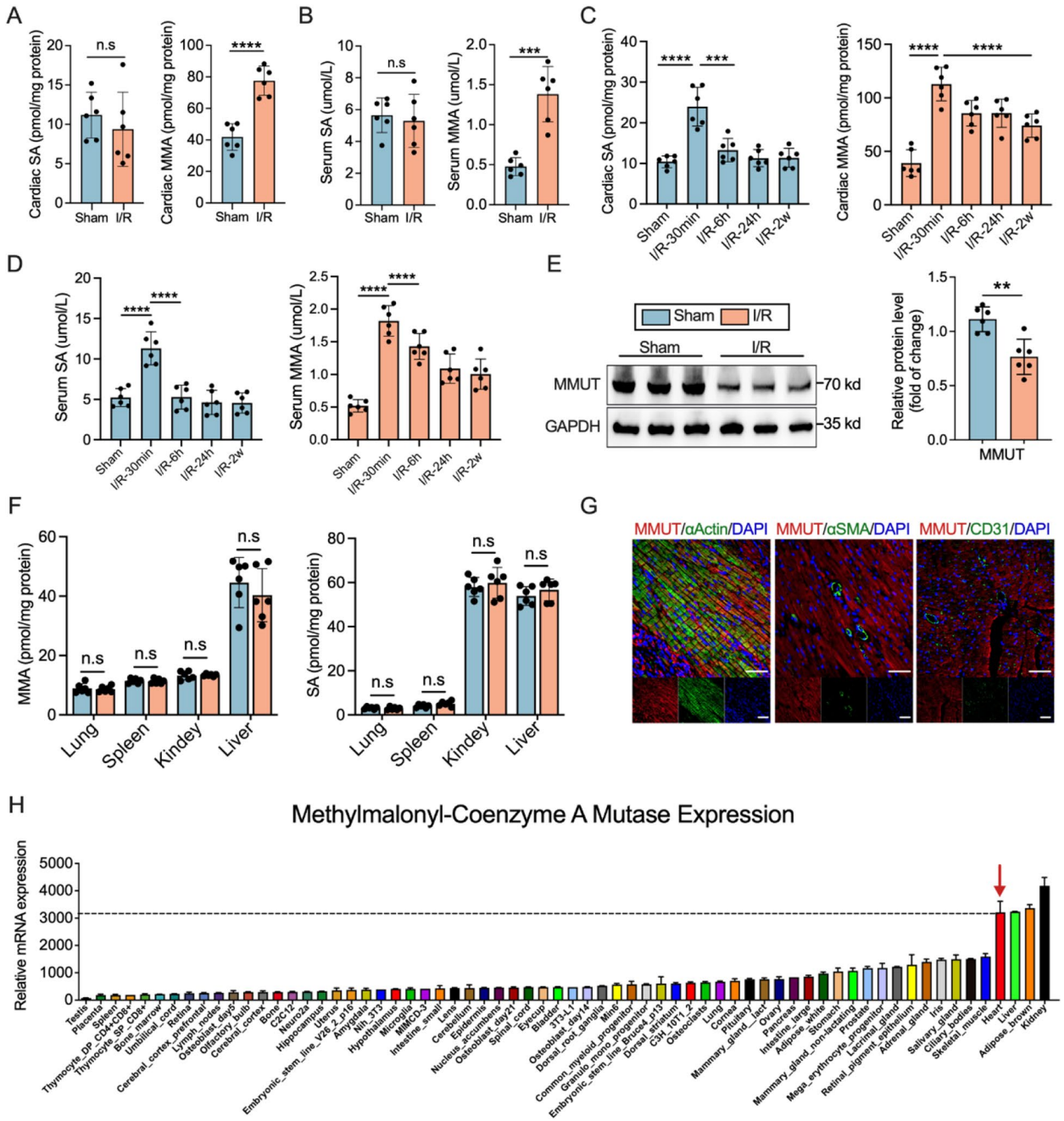


Fig. 2 Prolonged elevation of cardiac MMA in mice post-ischemia/reperfusion. **A** The levels of MMA and SA in the heart tissues of mice 24 h post-I/R ($n=6$). **B** The levels of MMA and SA in serum of mice 24 h post-I/R ($n=6$). **C** MMA and SA levels in the heart tissues of mice subjected to I/R surgery at serial time points ($n=6$). **D** MMA and SA levels in serum of mice after reperfusion at serial time points ($n=6$). **E** Western blots of the MMA metabolism-related enzyme MMUT in the heart tissues of mice after reperfusion for 24 h ($n=6$). **F** The levels of MMA and SA in other organs 24 h after myocardial reperfusion ($n=6$). **G** Cellular-specific expression of the MMUT protein in the heart tissues of mice 24 h after I/R injury, determined by immunofluorescence staining (top panel bar = 50 μm, bottom panel bar = 100 μm). **H** Methylmalonyl-coenzyme A mutase (*Mmut*) gene expression across multiple organs, tissues, and cells. The data were acquired from http://biogps.org/#goto=genereport&id=17850. Statistical significance was determined using Student's *t*-test (**A**, **B**, **E**, **F**) and 1-way ANOVA with Tukey's post hoc test (**C**, **D**); data are presented as the means ± SDs (*$P<0.05$; **$P<0.01$; ***$P<0.001$; ****$P<0.0001$; n.s., not significant)

severity of myocardial injury after 24 h of reperfusion, as assessed through TTC staining and serum CK-MB and LDH activity, while a comparable dose of DiSA administration did not significantly affect myocardial injury or ATP generation post-I/R (Additional file 1: Fig. S2A–H). These results suggest that MMA is involved in myocardial vulnerability and worsened cardiac dysfunction under I/R conditions, which is largely distinct from its isomer succinate.

To further confirm the role of endogenous MMA elevation, we established cardiomyocyte-specific *Mmut* knockout mice ($Mmut^{cko}$, Fig. 3A), validated by the protein expression of MMUT (Fig. 3B). Compared with $Mmut^{flox}$ homozygous ($Mmut^{fl/fl}$) littermates, cardiac and serum MMA levels were largely elevated in *Mmut*-deficient mice, whereas succinate levels were not obviously reduced (Fig. 3C and D), suggesting that methylmalonate is not an indispensable source of succinate. Consistent with the positive association between MMA and myocardial injury in humans (Fig. 1C), *Mmut* deficiency markedly increased infarct size (IS)/area at risk (AAR) ratio from 28 to 45% at 24 h post-I/R (Fig. 3E and F). Despite comparable heart function in *Mmut*-deficient mice and $Mmut^{fl/fl}$ littermates at 8 weeks of age, I/R-induced cardiac contractile dysfunction (indicated by decreased LVEF and LVFS) was further exacerbated in *Mmut*-deficient mice (Fig. 3G and H and Additional file 1: Table S4). Accordingly, cardiac apoptosis index in the border zone and serum CK-MB and LDH were also higher in *Mmut*-deficient mice than their $Mmut^{fl/fl}$ littermates (Fig. 3I–K). Consistent with the findings in males, female mice with *Mmut* deficiency also exhibited higher IA/AAR ratio and lower LVEF and LVFS post-I/R than their $Mmut^{fl/fl}$ littermates (Additional file 1: Fig. S3A–D). The impact of MMA accumulation on myocardial injury under I/R is not exclusive to females.

In addition to acute phase myocardial damage, MMA elevation also accelerated the progression of adverse remodeling at 7 days after I/R, as indicated by increased degrees of fibrosis, worsened ventricular dysfunction, and upregulated mRNA expression of fibrosis-related genes (Fig. 3L–O). Nonetheless, the potential for cardiac regeneration post-I/R was not significantly affected by Mmut ablation according to immunofluorescence staining of Ki67 and PH3 (Additional file 1: Fig. S4A–D). Taken together, MMA elevation is associated with increased myocardial vulnerability under I/R conditions compared to its isomer succinate.

Myocardial MMA elevation contributed to mitochondrial dysfunction post-ischemia/reperfusion

Posttranslational modifications (PTMs) are preferred for governing protein function because of their rapidity and low energy cost [37]. Considering the rapid changes in intracellular processes post-I/R, AC16 cardiomyocytes were treated with MMA for 4 h to observe the response of various types of PTMs. Overall, compared with minor changes in succinylation, malonylation, and ubiquitination, MMA increased the pan-acetylation of total proteins (Fig. 4A). Therefore, 4D-LFQ acetylproteomics was used to screen for hyperacetylated proteins and sites after adjusting for protein levels (Additional file 1: Fig. S5A–C). Overall, 4249 proteins and 13,234 sites were identified. As presented in the volcano plot, MMA treatment increased the acetylation of 143 proteins and decreased the acetylation of 67 proteins (Additional file 1: Fig. S5D). KEGG pathway analysis revealed enrichment of different proteins related to mitochondrial hemostasis, oxidative stress, energy metabolism, and RNA transcription processes (Fig. 4B–D and Additional file 1: S5E–I).

We subsequently investigated the impact of MMA elevation on mitochondrial microstructure and function in vitro and in vivo. Electron microscopy revealed that *Mmut* deficiency exacerbated morphological injuries to mitochondria in heart tissues post-I/R, including mitochondrial swelling, distortion, and mitochondrial crista fracture (Fig. 4E and F). ATP content in the border zone of I/R and sham hearts was lower in *Mmut*-deficient mice than $Mmut^{fl/fl}$ littermates (Fig. 4G). I/R-induced decreases in the activity of respiratory chain complexes in the I/R heart were more significant in *Mmut*-deficient mice than in $Mmut^{fl/fl}$ littermates, especially for complexes I, II, and V (Fig. 4H). A Seahorse XF Analyser revealed a dose-dependent decrease in basic and maximum oxygen consumption rates in AC16 cardiomyocytes treated with low and high doses of DiMMA, which was further validated in neonatal primary cardiomyocytes and isolated mitochondria from heart tissues post-I/R (Fig. 4I and J and Additional file 1: Fig. S6A–C). Moreover, MMA derivatives strongly impaired the mitochondrial membrane potential of AC16 cells (Fig. 4K). According to oxylipidomics analyses, *Mmut* deficiency greatly increased the lipid peroxidation of polyunsaturated fatty acids in the border zone of I/R hearts (Fig. 4L). Lipoxygenase metabolites with the highest variable importance, such as EETs, DiHDPEs, and DiHETs (Fig. 4L), have been reported to promote oxidative stress [38]. These findings indicated that MMA accumulation significantly exacerbates mitochondrial dysfunction in cardiomyocytes or heart tissues.

Impaired self-regulation of mitochondrial health in heart tissues due to I/R-induced MMA accumulation

We next assessed the impact of MMA accumulation on mitochondrial quality control system, an essential self-repair mechanism for maintaining mitochondrial

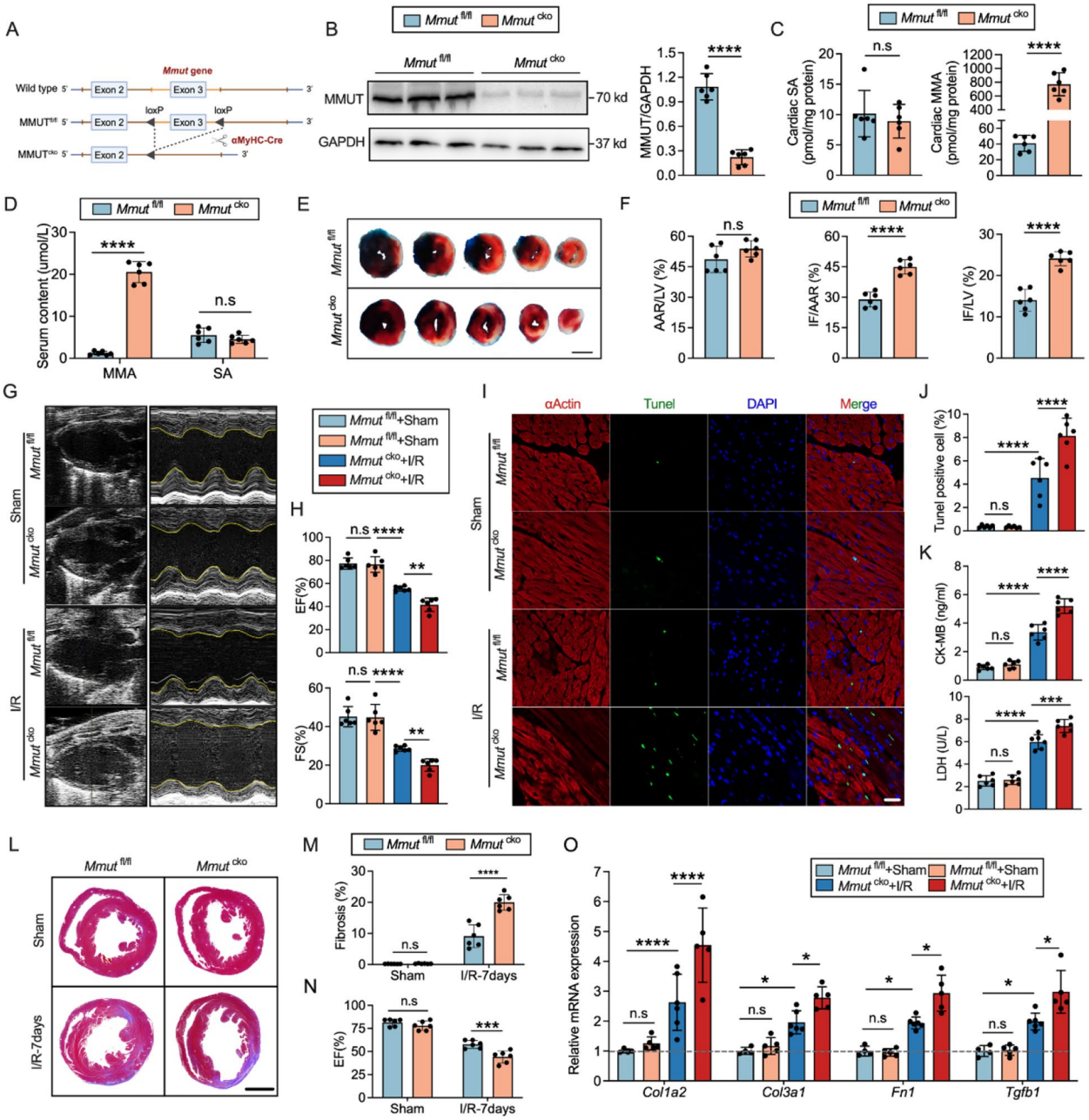


Fig. 3 Myocardial-specific *Mmut* knockout-induced endogenous MMA accumulation increases myocardial vulnerability during I/R. **A** Construction of myocardial-specific *Mmut* knockout mice. **B** MMUT protein expression in the heart tissues of $Mmut^{fl/fl}$ and $Mmut^{cko}$ mice ($n=6$). **C** MMA and SA contents in the hearts of $Mmut^{fl/fl}$ and $Mmut^{cko}$ mice ($n=6$). **D** Serum levels of MMA and SA in $Mmut^{fl/fl}$ and $Mmut^{cko}$ mice ($n=6$). **E** Evans blue and triphenyltetrazolium chloride (TTC) staining of heart sections from $Mmut^{fl/fl}$ and $Mmut^{cko}$ mice after reperfusion for 24 h (bar = 2 mm). **F** Quantification of the infarct area (IF), at-risk area (AAR), and left ventricle (LV) ($n=6$). **G** Representative images of left ventricular echocardiography. **H** The left ventricular ejection fraction (EF) and fractional shortening (FS) of $Mmut^{fl/fl}$ and $Mmut^{cko}$ mice 24 h after I/R surgery ($n=6$). **I**, **J** Representative TUNEL staining of heart sections and quantification of the apoptosis index (bar = 20 μm) ($n=6$). **K** Serum levels of the myocardial injury biomarkers CKMB and LDH in $Mmut^{fl/fl}$ and $Mmut^{cko}$ mice 24 h after I/R surgery ($n=6$). **L**, **M** Masson trichrome staining of heart sections from $Mmut^{fl/fl}$ and $Mmut^{cko}$ mice 7 days after I/R surgery and quantification of the fibrotic area (bar = 1 mm) ($n=6$). **N** Left ventricular ejection fraction (EF) of $Mmut^{fl/fl}$ and $Mmut.^{cko}$ mice 7 days post-I/R ($n=6$). **O** mRNA expression of cardiac fibrosis-related genes in the heart tissues of mice 7 days post-I/R ($n=6$). Statistical significance was determined via Student's *t*-test (**B**, **C**, **D**, **F**, **M**, **N**), and 1-way ANOVA and Tukey's post hoc analysis (**H**–**K**, **O**). The data are presented as the mean ± SD (*$P<0.05$; **$P<0.01$; ***$P<0.001$; ****$P<0.0001$; n.s., not significant)

hemostasis under stress [39]. After 24 h of reperfusion, the number of mitochondria, particularly vacuolated mitochondria, was greater in the border zone of *Mmut*-deficient mice than WT littermates (Fig. 5A and B). Myocardial I/R is accompanied by stress-induced hyperglycemia, lactic acid accumulation, and other energy metabolism disorders. We observed that the MMA derivatives DiMMA and DeMMA strongly promoted greater increase in mitochondrial mass in AC16 cells than did additional exposure to glucose, lactate, succinate, and homocysteine, as assessed by mtDNA/nDNA ratio and the intensity of MitoTracker Green (Fig. 5C and D). In vivo, *Mmut* deficiency increased the levels of mitochondrial proteins in I/R hearts compared with those in $Mmut^{fl/fl}$ control hearts (Additional file 1: Fig. S7A).

Despite the increased mtDNA abundance induced by MMA, the mRNA expression of mtDNA-encoded genes was especially decreased in *Mmut*-deficient mice compared with WT littermates (Fig. 5E). The expression of mitochondrial biogenesis-related genes, such as *PGC-1α*, *NRF-1*, and *TFAM*, did not increase but decreased significantly in AC16 cells after DiMMA treatment (Fig. 5F). These findings indicate that excessive MMA impairs mitochondrial biosynthesis in the I/R heart.

Given that clearing impaired mitochondria through mitochondrial autophagy/mitophagy is essential for maintaining mitochondrial homeostasis, we further investigated mitochondrial autophagy/mitophagy. *Mmut* deficiency increased the susceptibility to excessive mitochondrial fission in heart tissues of I/R mice, despite a minor effect on mitochondrial fusion (Additional file 1: Fig. S7B). Moreover, I/R promoted the recruitment of LC3 and p62 to mitochondria, whereas *Mmut* deficiency compromised this alteration in the border zone of heart tissues after 24 h of I/R (Fig. 5G–I). According to the time sequence analysis, mito-LC3 and mito-p62 levels were lower in *Mmut*-deficient hearts in the first 6 h post-I/R and then decreased more rapidly than WT mice (Fig. 5J and K). These results suggest that MMA inhibits the activation of mitochondrial autophagy/mitophagy to assimilate impaired mitochondria, which is responsible for the additional accumulation of damaged mitochondria post-I/R.

We further validate whether impaired mitochondrial autophagy/mitophagy is indispensable for MMA-induced mitochondrial dyshomeostasis. Carbonyl cyanide p-trichloromethoxyphenylhydrazone (CCCP) was used to induce mitochondrial depolarization and activate mitophagy without affecting macroautophagy [40]. CCCP increased the mitochondrial localization of LC3 and p62 in heart tissues, whereas *Mmut* deficiency substantially dampened this change (Additional file 1: Fig. S7C and D). The expression of mTORC1 complex FIP200 and Atg13, reflecting autophagosome biogenesis, was not reduced but was moderately elevated by DiMMA treatment in AC16 cells (Additional file 1: Fig. S7E and F). Moreover, the expression of LAMP1 and RAB7 as well as LysoTracker intensity were not affected by DiMMA treatment (Additional file 1: Fig. S7E–G). Thus, MMA-induced insufficient assimilation of damaged mitochondria was not attributed to the biogenesis of autophagosomes and lysosomes or autophagosome–lysosome fusion. Collectively, these data suggest that the harmful effect of MMA on mitochondrial quality control may be mediated, at least in part, by inhibiting an intermediate hub of the mitochondrial autophagy/mitophagy process under I/R conditions.

BNIP3 overexpression alleviates mitochondrial and myocardial injury related to MMA elevation

We further analyzed the classical and nonclassical signals of mitophagy, including Parkin, BNIP3, FUNDC1, NIX, and RAB9 [6]. These mitophagy-related proteins increased at 4 h after reperfusion but markedly decreased at 24 h after I/R. Notably, elevated BNIP3 expression during the acute phase of I/R was significantly lower in *Mmut*-deficient mice than $Mmut^{fl/fl}$ littermates (Fig. 6A). In vitro, DiMMA treatment inhibited BNIP3 mRNA expression in AC16 cells under hypoxia reoxygenation (H/R) conditions (Fig. 6B).

(See figure on next page.)

Fig. 4 MMA promotes mitochondrial damage and oxidative stress in myocardial I/R injury. **A** PTMs of total proteins in AC16 cells treated with methylmalonic acid (MMA) for 4 h. **B** The top 16 enriched KEGG pathways associated with the differentially acetylated proteins. **C**, **D** Gene Ontology analysis and heatmap of mitochondria-related differentially expressed proteins from acetylproteomics. **E** Representative electron microscopy images (15,000×) of heart sections. Representative impaired mitochondria are indicated by red arrows (bar = 500 nm). **F** Quantification of mitochondria with disorganized cristae ($n = 6$). **G** ATP contents in heart tissues 24 h after I/R ($n = 6$ per group). **H** Relative cardiac activities of mitochondrial respiratory chain complexes I, II, III, IV, and V in $Mmut^{fl/fl}$ and $Mmut^{cko}$ mice 24 h after I/R ($n = 6$ per group). **I**, **J** The mitochondrial oxygen consumption rate (OCR) in AC16 cells treated with low (50 μM/24 h) or high (100 μM/24 h) DiMMA concentrations was measured via a Seahorse trace ($n = 4$). **K** Representative images of JC-1 staining for the detection of the mitochondrial membrane potential in AC16 cells ($n = 6$). **L** Oxylipin profiles in the heart tissues of $Mmut^{fl/fl}$ and $Mmut^{cko}$ mice 24 h after I/R surgery. Statistical significance was determined via 1-way ANOVA (**F**, **G**, **K**) or 2-way ANOVA (**H**, **I**, **J**) and Tukey's post hoc analysis. All data are presented as the mean ± SD (*$P < 0.05$; **$P < 0.01$; ***$P < 0.001$; ****$P < 0.0001$; n.s., not significant)

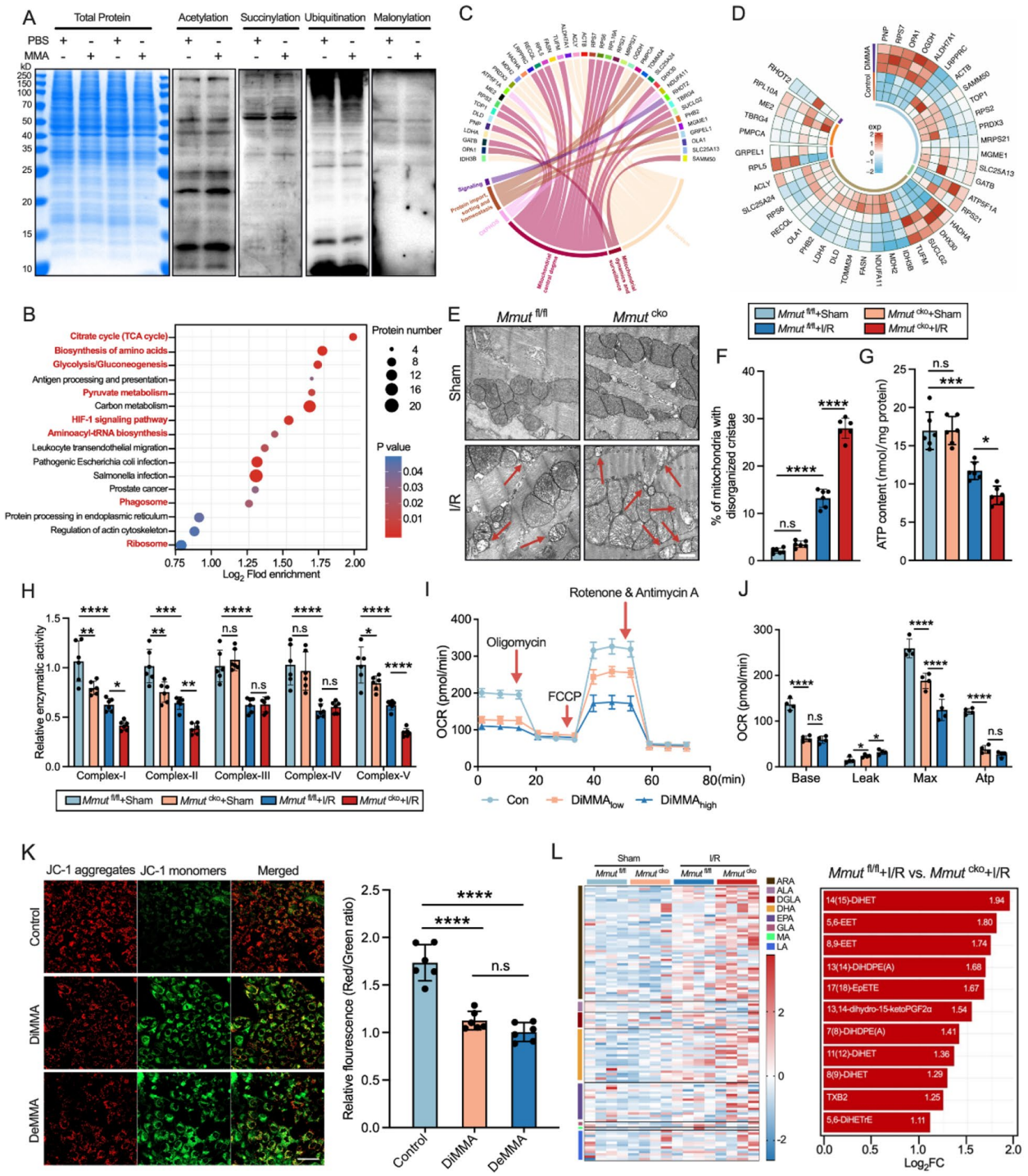


Fig. 4 (See legend on previous page.)

We then investigated whether improving BNIP3-mediated mitochondrial autophagy/mitophagy is a critical mechanism against MMA-related myocardial and mitochondrial vulnerability. To this end, cardiac BNIP3 was overexpressed in *Mmut*-deficient mice by injecting AAV9-BNIP3 driven by the troponin T promoter (Fig. 6C and D and Additional file 1: Fig. S8A). Cardiac H_2O_2 and MDA products in *Mmut*-deficient mice post-I/R were alleviated by BNIP3 overexpression, whereas MMUT protein and MMA contents were unchanged

(Additional file 1: Fig. S8B–E). AAV9-BNIP3 injection alleviated the decreases in LVEF and LVFS, and the increases in serum CK-MB and LDH levels as well as IS/AAR ratio after 24 h of reperfusion, especially in *Mmut*^{cko} mice (Fig. 6E–I and Additional file 1: Table S5). Accordingly, BNIP3 overexpression largely counteracted the harmful effects of MMA accumulation on mitophagy and mitochondrial quality (Fig. 6J–L and Additional file 1: Fig. S8F and G).

Although BNIP3 has dual effects on promoting apoptosis and mitophagy [41], we noted that BNIP3 overexpression did not significantly increase the apoptosis index or ratio of cleaved/total caspase-3 in heart tissues (Additional file 1: Fig. S8H–J). Treatment with 3-MA, a nonspecific autophagy/mitophagy inhibitor [40], decreased the expression of mitochondrial LC3II and p62 in BNIP3-overexpressing hearts post-I/R (Fig. S8K). As expected, the protective effect of BNIP3 on MMA accumulation-related myocardial vulnerability was abolished by 3-MA treatment (Fig. S8L). These data suggested that BNIP3 overexpression may improve MMA-related myocardial vulnerability and mitochondrial dyshomeostasis post-I/R by rescuing impaired mitophagy.

Hyperacetylation of CREB^{K309} in MMA-mediated inhibition of BNIP3 promoter activity in I/R hearts

Given that MMA accumulation decreased BNIP3 protein and mRNA expression (Fig. 5A–C), we next investigated how MMA accumulation reduces the mRNA expression of BNIP3. Dual luciferase reporter assays confirmed that DiMMA treatment inhibited the transcriptional activity of BNIP3 promoter in AC16 cells (Fig. 7A). Given the increased pan-acetylation under MMA treatment (Fig. 4A), we speculated that MMA may increase the acetylation of transcription factors, thereby inhibiting the activity of the promoter [37]. By overlapping the in silico transcription factor database with MMA-induced hyperacetylated proteins in acetylproteomics, we identified CREB as a possible unheeded transcription factor for BNIP3 expression (Fig. 7B and C).

We depicted the time-dependent changes in acetylated CREB, BNIP3, and ROS generation in I/R hearts during the initial 24 h. Interestingly, cardiac H_2O_2 contents were significantly elevated with two stages, including 0.5 h and 12 h after reperfusion (Additional file 1: Fig. S9A). Acetylated CREB continuously increased after 30 min of reperfusion, while BNIP3 expression was increased after 2 h reperfusion and largely declined after 12 h of I/R. CREB acetylation had a faster and higher increase and BNIP3 expression was largely inhibited throughout the whole I/R process in Mmut-deficient mice, compared to their wild-type littermates (Additional file 1: Fig. S9B–D). CREB was distributed primarily in the nucleus of AC16 cells which was not affected by DiMMA treatment (Fig. S10A). Nonetheless, CREB knockdown largely attenuated the increase in BNIP3 expression induced by *MMUT* overexpression in AC16 cells post-H/R (Fig. 7D and Additional file 1: Fig. S10B). Consistent with acetylproteomic analysis, CREB acetylation was significantly greater in heart tissues of *Mmut*-deficient mice post-I/R compared with *Mmut*$^{fl/fl}$ mice (Fig. 7E and Additional file 1: Fig. S10C). In vitro, DiMMA treatment upregulated CREB acetylation in a dose-dependent manner (Additional file 1: Fig. S10D and E). These data suggest that CREB hyperacetylation is involved in the process that MMA inhibits the initiation of BNIP3 transcription.

We next confirmed the interaction between hyperacetylation of CREB and BNIP3 promoter. Mass spectrometry analysis revealed that lysine (K) residues 309 and 325 were the major sites of CREB hyperacetylation under MMA treatment (Fig. 7F). Both sites were highly conserved across species, including *Homo sapiens* (Fig. 7G). Subsequently, we mutated the two K residues in CREB using arginine (R) to mimic a protein deacetylation state and glutamine (Q) to mimic a protein hyperacetylation state. Compared with CREB^{WT}, the CREB^{K309R}

(See figure on next page.)

Fig. 5 MMA accumulation aggravates the disruption of mitochondrial quality control in myocardial I/R injury. **A**, **B** Representative electron microscopy images of heart sections 24 h after I/R surgery (top panel bar = 500 nm, bottom panel bar = 250 nm), and quantification of the average number of mitochondria and the number of mitochondria with disorganized cristae from A ($n = 6$). **C**, **D** Mitochondrial mass assessed by the mtDNA/nDNA ratio and MitoTracker Green staining in AC16 cells after treatment with each metabolite for 24 h ($n = 3$). **E** mRNA expression of nuclear-encoded and mitochondrial-encoded electron transport chain genes in heart tissues of *Mmut*$^{fl/fl}$ and *Mmut*^{cko} mice 24 h after I/R surgery ($n = 4$). **F** Quantitative polymerase chain reaction analysis of the mRNA levels of the mitochondrial biogenesis-related genes *PGC-1α*, *TFAM*, *NRF1*, *ND6* and *ATP6* in AC16 cells ($n = 4$–6). **G**, **H** Western blot analysis and quantification of the mitochondrial autophagy/mitophagy markers LC3 and p62 in isolated heart mitochondria from *Mmut*$^{fl/fl}$ and *Mmut*^{cko} mice 24 h after I/R surgery ($n = 6$). **I** Immunofluorescence staining of TOM20/LC3 in the heart tissues of mice 24 h after myocardial reperfusion injury (bar = 20 μm). **J**, **K** Mitochondrial LC3 in the heart tissues of *Mmut*$^{fl/fl}$ and *Mmut*^{cko} mice at different time points after I/R surgery ($n = 6$). Statistical significance was determined via Student's *t*-test (**B**, **F**), and 1-way ANOVA (**C**, **D**, **E**, **H**), or 2-way ANOVA (**K**) and post hoc analysis. The data are presented as the means ± SDs (*$P < 0.05$; **$P < 0.01$; ***$P < 0.001$; ****$P < 0.0001$; n.s., not significant)

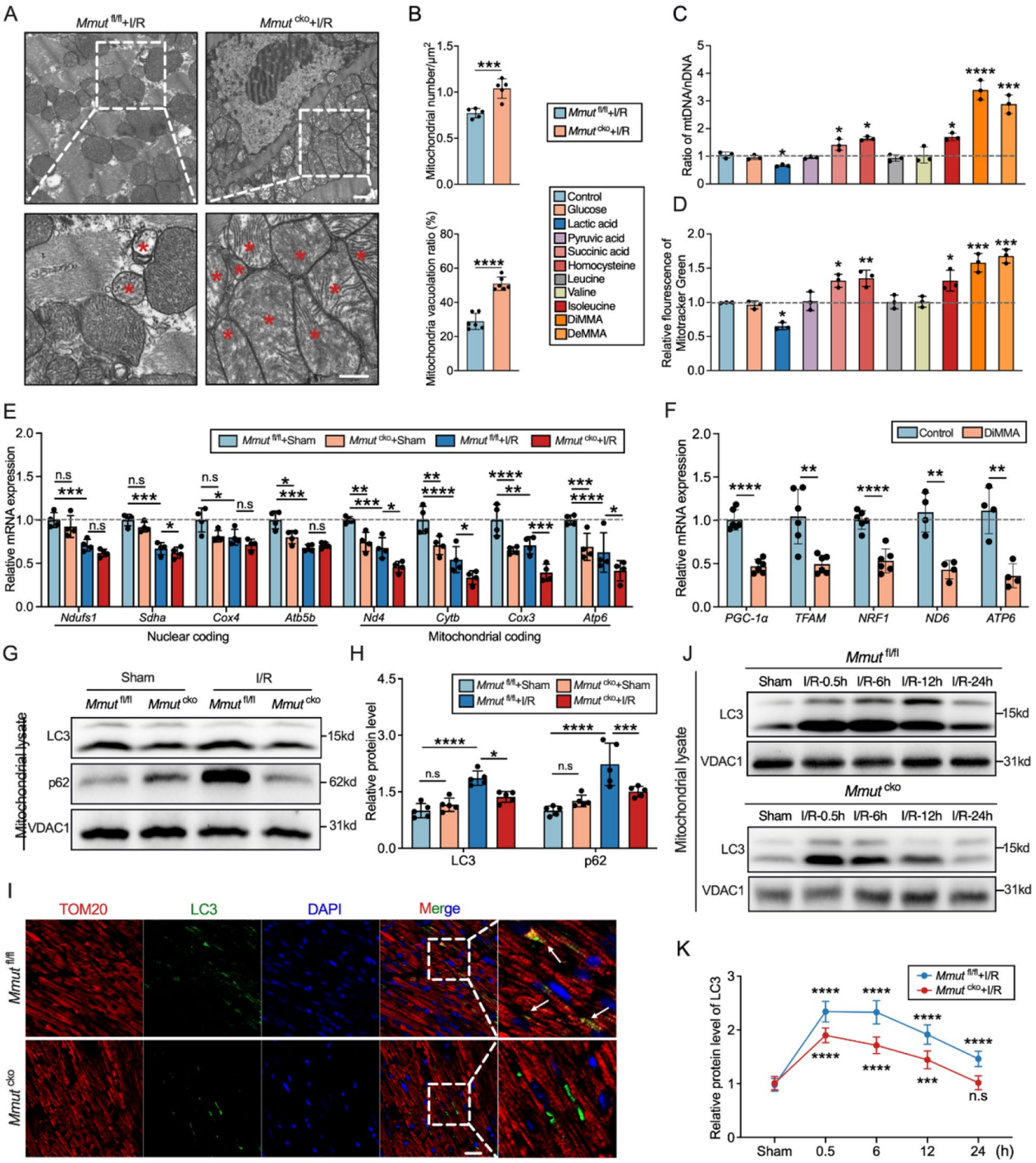


Fig. 5 (See legend on previous page.)

mutant increased and CREB^{K309Q} inhibited the activity of the BNIP3 promoter in vitro, whereas CREB^{K325R} and CREB^{K325Q} did not significantly affect BNIP3 promoter activity (Fig. 7H). In silico analysis revealed two potential CREB-responsive domains within the proximal region of BNIP3 promoter at positions between − 498 and − 487 bp and between − 300 and − 289 bp. ChIP assays confirmed that the binding between CREB and both segments of BNIP3 promoter region was lower in *Mmut*-deficient mice than WT mice (Fig. 7I and J). The

interaction was repeatable in HEK 293 cells transfected with plasmids containing WT or mutant CREB with a flag (Fig. 7K). To determine the functional sites in the BNIP3 promoter, each segment in the BNIP3 promoter was deleted (Fig. 7L). Dual luciferase reporter assays confirmed that loss of the region between −300 and −289 bp impedes the function of CREB to activate BNIP3 promoter (Fig. 7M). Overall, MMA-induced $CREB^{K309}$ hyperacetylation hinders binding to cis-elements located between −300 and −289 bp of the BNIP3 promoter, thereby inhibiting BNIP3 transcription.

We investigated the underlying mechanism of MMA-induced CREB hyperacetylation. Although acetylation can occur through nonenzymatic mechanism dependent on the bioavailability of acetyl-CoA [37], *Mmut* deficiency did not increase acetyl-CoA levels in heart tissues post-I/R compared with $Mmut^{fl/fl}$ mice (Additional file 1: Fig. S10F). The seven sirtuin family members are well-established deacetylases regulating nonhistone protein acetylation [37], whereas only sirtuin 1 (SIRT1) was significantly decreased in heart tissues of *Mmut*-deficient mice post-I/R compared with $Mmut^{fl/fl}$ littermates (Additional file 1: Fig. S10G). This finding was further confirmed by the assessment of SIRT1 activity (Fig. 7N). Considering that SIRT1 and SIRT2 participate in the acetylation of transcription factors [37], we overexpressed SIRT1 and SIRT2 in AC16 cells and observed that the upregulation of SIRT1, not SIRT2, promoted CREB deacetylation, BNIP3 expression, and mitophagy activity under MMA treatment (Fig. 7O). These findings collectively support that MMA elevation inhibits the SIRT1-mediated deacetylation of the transcription factor $CREB^{K309}$, which blocks the initiation of BNIP3 expression and compromises the response of mitochondrial quality control to I/R attack.

Therapeutic potential of targeting MMA metabolism in porcine with myocardial ischemia/reperfusion

To evaluate the translational value of targeting mitochondrial MMA metabolism against myocardial I/R injury, we established a porcine model of *MMUT* overexpression followed by I/R operation (Fig. 8A). Twelve pigs were randomly assigned to receive AAV9-*MMUT* or AAV9-vector 4 weeks before I/R surgery. Two animals died of ventricular fibrillation during the I/R operation and no fatalities occurred during the 4-week after I/R. Echocardiographic indices of fractional shortening were comparable before and after AAV9 injection (Additional file 1: Fig. S11A). After 4 weeks of I/R, MMUT protein levels in hearts subjected to AAV9-*MMUT* injection nearly doubled (Fig. 8B and Additional file 1: Fig. S11B and C). *MMUT* overexpression reduced serum MMA concentration in the acute phase (3 days) and chronic phase (28 days) post-I/R (Fig. 8C). CMR assessment at 3 days post-I/R showed comparable AAR between both groups, whereas Mmut overexpressing pigs presented a significantly reduced infarct size and mass (Fig. 8D and E and Additional file 1: Fig. S11D and Table S6). Consistently, *MMUT* overexpression improved contractile dysfunction and decreased TnI and CK-MB levels (Fig. 8G and H and Additional file 1: Fig. S11E and F). Histological analysis showed partial amelioration of pathological remodeling and abnormal mitochondrial microstructure in heart sections following *MMUT* delivery (Fig. 8I–K and Additional file 1: Fig. S11G). According to proteomic analysis of both groups, the differentially expressed proteins were significantly enriched in processes related to mitochondrial homeostasis, oxidative stress, and energy metabolism (Fig. 8L). Together, these findings obtained from a large animal model provide preclinical evidence that *MMUT* delivery enhances mitochondrial

(See figure on next page.)

Fig. 6 BNIP3 overexpression ameliorates impaired mitochondrial quality in *Mmut*-deficient hearts after I/R injury. **A** Western blot analysis and quantification of classical and alternative mitophagy pathway-related proteins (BNIP3, PARKIN, FUNDC1, NIX, and RAB9) in $Mmut^{fl/fl}$ and $Mmut^{cko}$ mice after I/R surgery ($n=6$). **B** BNIP3 mRNA expression in AC16 cells with *MMUT* inhibition and hypoxia reoxygenation treatment ($n=6$). **C** Experimental design of this study. Eight-week-old $Mmut^{fl/fl}$ and $Mmut^{cko}$ littermates were injected via the caudal vein with AAV9-BNIP3 or AAV9–empty vector. After 4 weeks, I/R injury was induced for further experiments. **D** Western blots showing BNIP3 expression in the heart tissues of wild-type mice subjected to I/R surgery after reperfusion for 24 h. **E** Representative M-mode and B-mode echocardiographic images of the left ventricle from $Mmut^{fl/fl}$ and $Mmut^{cko}$ mice that received AAV9-BNIP3 or AAV9–empty vector 24 h after I/R surgery. **F** Quantification of left ventricle ejection fraction (EF) and fractional shortening (FS) ($n=8$). **G** Serum levels of the myocardial injury biomarkers lactate dehydrogenase (LDH) and CKMB in $Mmut^{fl/fl}$ and $Mmut^{cko}$ mice with BNIP3 overexpression 24 h after I/R surgery ($n=6$). **H**, **I** Representative images of Evans blue and triphenyltetrazolium chloride (TTC) staining of heart sections from $Mmut^{fl/fl}$ and $Mmut^{cko}$ mice with BNIP3 overexpression after reperfusion for 24 h and the quantification of the infarct area (IF), at-risk area (AAR), and left ventricle (LV) ($n=6$) (bar = 2 mm). **J** ATP levels in the heat-exposed tissues of $Mmut^{fl/fl}$ and $Mmut^{cko}$ mice with BNIP3 overexpression after reperfusion for 24 h ($n=6$). **K** Representative electron microscopic images of heart sections 24 h after I/R surgery (bar = 1 μm). **L** Relative cardiac activities of mitochondrial respiratory chain complexes I, II, III, IV, and V of $Mmut^{fl/fl}$ and $Mmut^{cko}$ mice that received AAV9-BNIP3 or AAV9–empty vector 24 h after I/R surgery ($n=6$ per group). Statistical significance was determined via 1-way ANOVA (**B**, **F**, **G**, **I**, **J**) or 2-way ANOVA (**A**, **L**) and post hoc analysis. The data are presented as the means ± SDs (*$P<0.05$; **$P<0.01$; ***$P<0.001$; ****$P<0.0001$; n.s., not significant)

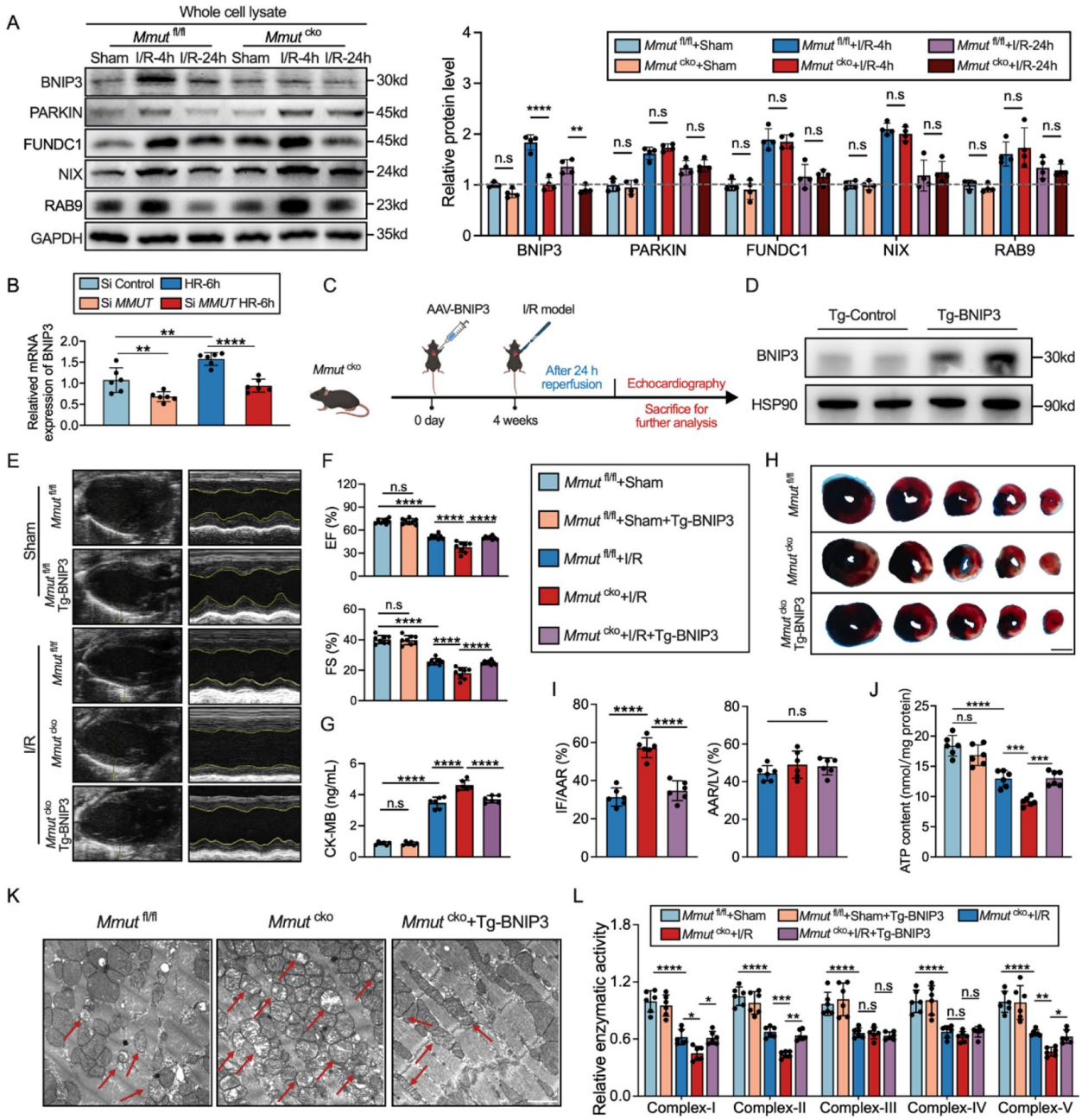


Fig. 6 (See legend on previous page.)

MMA metabolism, suggesting a promising strategy for mitigating myocardial reperfusion injury and adverse remodeling.

Discussion

Dysregulated mitochondrial metabolism is one of the most prominent features of the myocardium following I/R. A major question arises regarding how emerging mitochondrial knowledge can be translated into clinical practice [42]. We revealed that mitochondrial metabolite MMA, which is largely distinct from its well-known isomer succinate, is a promising prognostic biomarker and a pathogenic factor aggravating myocardial vulnerability and mitochondrial dysfunction post-I/R. Mechanistically, MMA promoted hyperacetylation of the transcription factor CREB^{K309} partly by inhibiting the activity of the deacetylase SIRT1. CREB^{K309} hyperacetylation weakened its binding to the BNIP3 promoter region, thereby

inhibiting BNIP3 expression and the regulation of mitochondrial quality control. Furthermore, AAV9-mediated *MMUT* overexpression reduced myocardial MMA accumulation, mitochondrial impairment, and myocardial vulnerability in a porcine I/R model. These findings provide translational evidence that targeting mitochondrial MMA metabolism holds promise as a novel therapeutic target and prognostic biomarker in patients with AMI.

MMA and succinate have close biological links through the conversion of methylmalonyl-CoA to succinyl-CoA by *MMUT* [7]. Several experimental studies have confirmed that succinate levels increase during the ischemic period which is simultaneously metabolized upon reperfusion. This process is accompanied by excess mitochondrial ROS production, contributing to myocardial injury [43–46]. Compared with the rapid decrease in succinate levels after reperfusion, elevated MMA levels persisted for more than 24 h. Our findings align with previous reports that ischemia-induced succinate accumulation in the heart ex vivo is rapidly restored to normoxic levels within 5 min of reperfusion due to the recovery of succinate dehydrogenase activity after reperfusion [43]. Our previous community-based cohort analyses first established a robust association between MMA and cardiovascular mortality [8, 13], which has been recently validated in WECAC and NORVIT studies [47]. The longitudinal association of MMA with HF risk post-MI was unknown. Herein, we further reported that MMA, which outmatches succinate, exhibits excellent performance in discriminating the risk of 1-year incident HF post-MI. Owing to the limited sample size and potential confounding factors, future large-scale studies are needed for validation. Overall, our findings suggest that MMA may be a prognostic biomarker related to mitochondrial status for cardiovascular risk stratification, compared with its well-known isomer succinate. The underestimated value of MMA may be partly due to the challenging chromatographic separation between the isomers MMA and succinate [35, 48].

The impact of MMA accumulation is largely unknown in the cardiovascular field. Unexpectedly, we detected robust expression of MMUT, a core mitochondrial enzyme involved in methylmalonate metabolism, in heart tissues, which are among the four organs with the highest *Mmut* expression. Interestingly, we noted that the circulating concentration of succinate was greater than that of MMA in humans and mice; however, conversely, the content of MMA in myocardial tissue largely exceeded that of succinate. This finding is in line with previous reports that MMA has poor cellular membrane permeability [25], which might be related to its branched structure and polarity. Overall, heart is endowed with an active flux of MMA metabolism, rendering it susceptible to MMA accumulation when this process is blocked under pathological conditions.

In the present study, myocardium-specific *Mmut* knockout and overexpression provided biological evidence that endogenous MMA accumulation exacerbates mitochondrial and myocardial vulnerability under I/R conditions. Previous biological studies regarding MMA metabolism have focused mainly on nerves and kidneys to explain the harms of methylmalonic acidemia [49]. Indeed, congenital heart disease and HF were recently reported as late-onset manifestations in patients with methylmalonic acidemia [10, 11]. This may be explained by different tolerances across organs in response to MMA exposure. For example, liver is the dominant organ of MMA metabolism, but liver injury is not the main

(See figure on next page.)

Fig. 7 MMA inhibits BNIP3-mediated mitochondrial quality control by promoting $CREB^{K309}$ hyperacetylation to reduce its transcriptional activity. **A** Dual luciferase activity of BNIP3 in AC16 cells treated with or without dimethyl methylmalonate (DiMMA) and subjected to H/R injury. **B** The top 10 of upregulated acetylated proteins. **C** Chromatin immunoprecipitation-sequencing data showing the binding of CREB and H3K27ac on the BNIP3 promoter according to silica analysis (accession codes #GSE99895 for CREB and GSE73769 for H3K27Ac). **D** Western blot analysis of BNIP3 in AC16 cells after treatment with CREB siRNA or a plasmid containing the *MMUT* gene for 48 h and then treatment with 50 μM DiMMA for another 24 h ($n = 6$). **E** The acetylation levels of CREB were measured in lysates of heart tissue from $Mmut^{fl/fl}$ and $Mmut^{cko}$ mice 24 h after I/R ($n = 6$). **F** The mass spectrum of the acetylized peptide from CREB identified different residues, K309 and K325, in DiMMA-treated AC16 cells. **G** Sequence alignment analysis of K309 and K325 of CREB across species. **H** Luciferase activity of the BNIP3 promoter in HEK 293 cells with different types of CREB mutants ($n = 6$). Both K residues (K309 and/or K325) in CREB were mutated to arginine (R) for a protein deacetylation state mimic or to glutamine (Q) for a protein hyperacetylation state mimic. **I**, **J** Chromatin immunoprecipitation (ChIP) analysis and quantification of BNIP3 promoter regions (−498 to −487 bp and −300 to −289 bp) in the lysates of heart tissues from $Mmut^{fl/fl}$ and $Mmut^{cko}$ mice with an anti-CREB antibody ($n = 6$). **K** ChIP analysis of HEK 293 cells with each flag-CREB mutant (K309Q, K309R, K325Q, and K325R, $n = 3$). The precipitated chromatin covering both potential binding regions of BNIP3 promotor and the transcription region as controls. **L** Construction of site-directed mutations in two regions of the BNIP3 promoter (Mut1, Mut2, and Mut1/2). **M** Dual luciferase activity of the wild-type and mutated BNIP3 promoters in HEK 293 cells ($n = 6$). **N** SIRT1 enzyme activity in the heart tissue lysates ($n = 4$). **O** Western blot analysis and quantification of the protein levels of mito-LC3, mito-p62, acetylated CREB, and BNIP3 in AC16 cells transfected with SIRT1- or SIRT2-overexpressing cells for 48 h and then treated with dimethyl methylmalonic acid (DiMMA) for another 24 h ($n = 6$). Statistical significance was determined via 1-way ANOVA and multiple-comparison post hoc analysis. Data are presented as the means ± SD (*$P < 0.05$; **$P < 0.01$; ***$P < 0.001$; ****$P < 0.0001$; n.s., not significant)

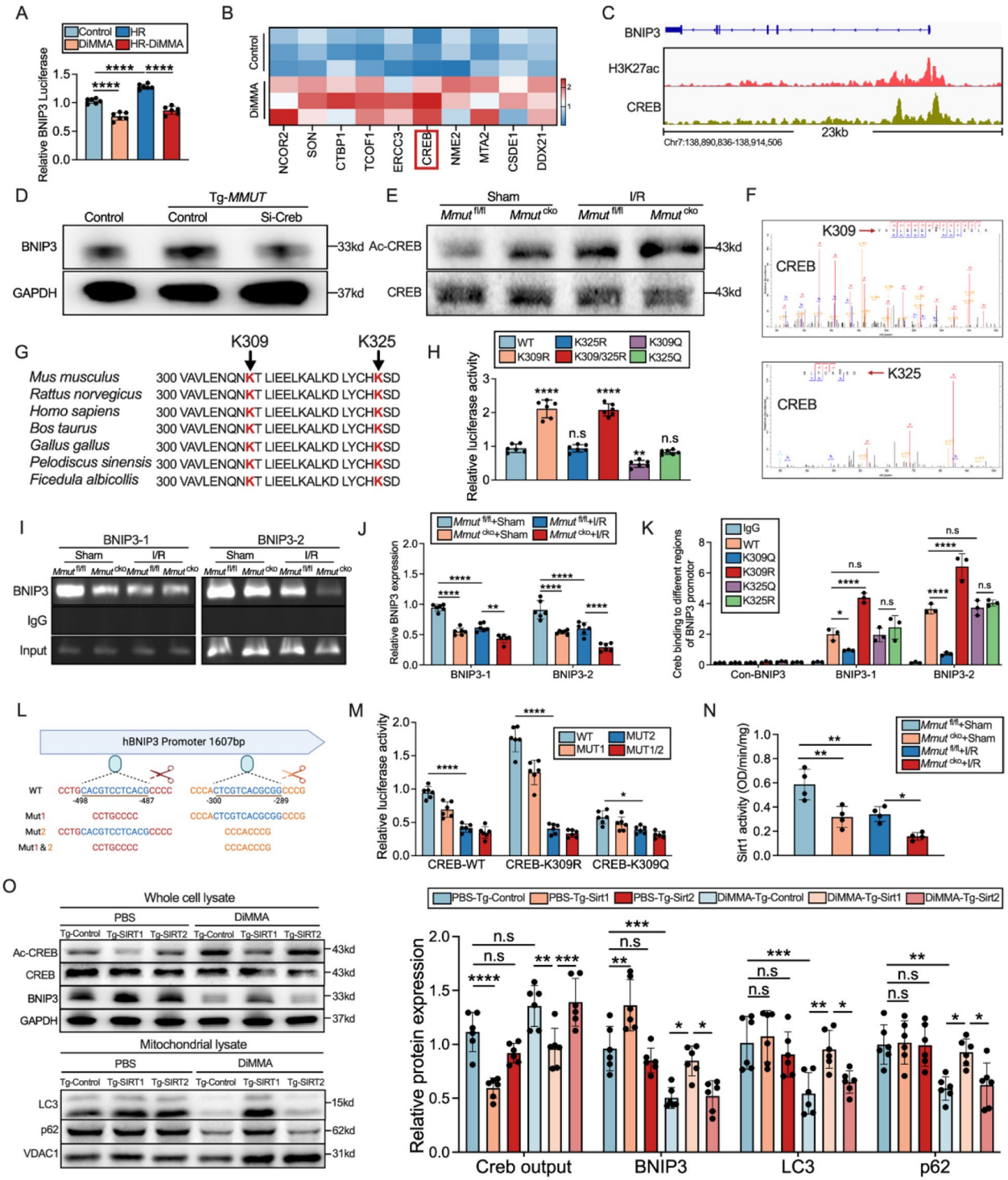


Fig. 7 (See legend on previous page.)

manifestation of inborn methylmalonic acidemia. Overall, this translational study expands the clinical relevance of MMA from inherited disease to the management of cardiovascular disease.

Vitamin B12 supplementation has been shown to lower MMA levels among individuals with B12 deficiency [12]. However, cumulative evidence suggests that a considerable proportion of adults with elevated MMA levels have

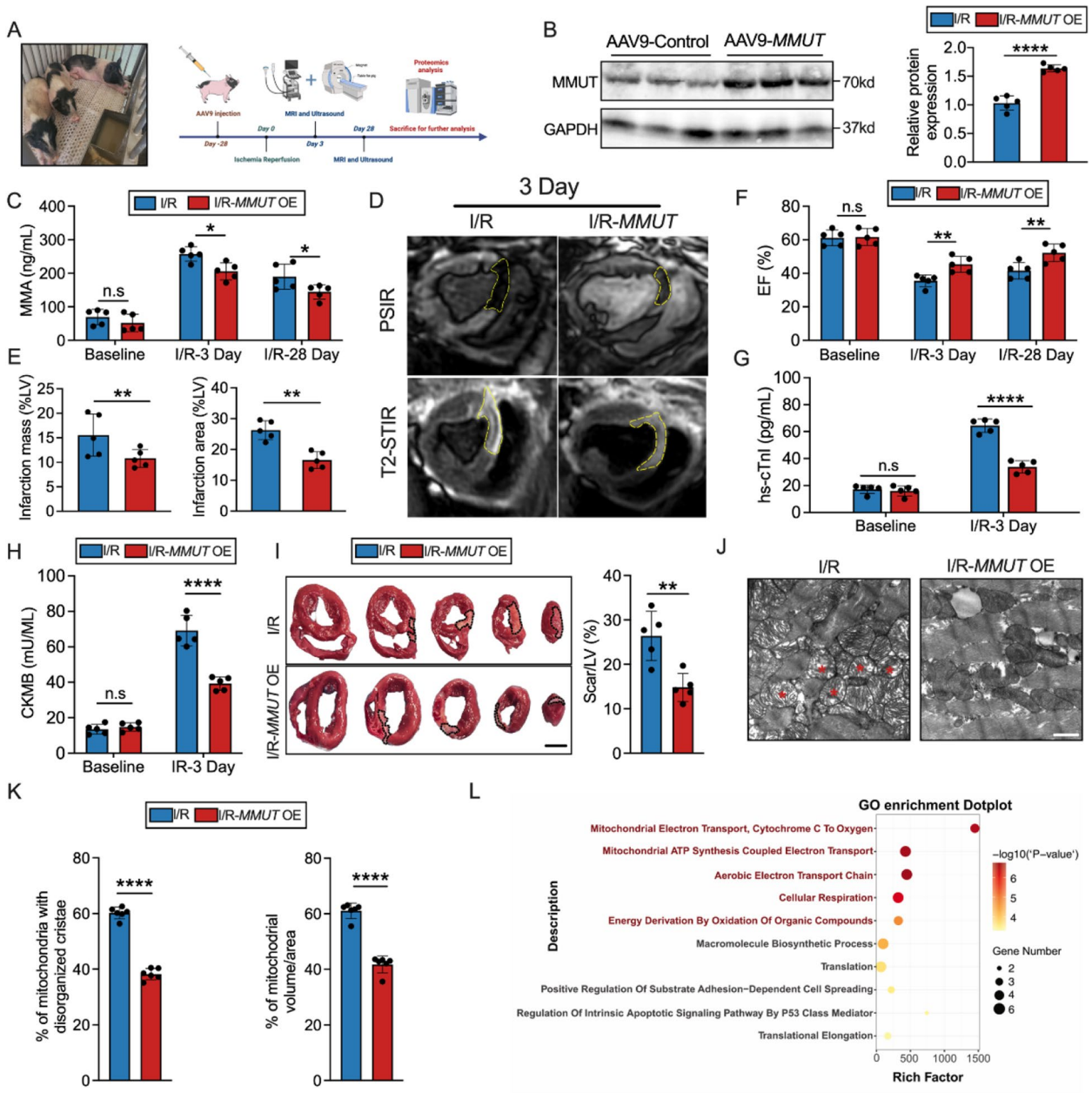


Fig. 8 *MMUT* delivery via adeno-associated virus serotype 9 significantly improves methylmalate metabolism and cardiac phenotypes in pigs subjected to I/R injury. **A** Schematic study design. Adeno-associated virus serotype 9 (AAV9), encoding the human *MMUT* gene, or an empty vector was locally injected into the hearts of male Bama miniature pigs (25 to 30 kg, 4 months of age) to induce cardiac overexpression. Four weeks after transfection, a porcine model of I/R injury was established. **B** Western blot analysis and quantification of MMUT protein expression ($n = 5$). **C** Serum MMA levels at baseline and at different time points after I/R injury ($n = 5$). **D**, **E** Representative cardiac magnetic resonance imaging (CMR) images of edema and the infarct size (day 3). Quantification of the infarct mass and infarct size ($n = 5$). **F** Quantification of the ejection fraction based via CMR ($n = 5$). **G**, **H** Serum levels of the myocardial injury biomarkers CKMB and hs-cTnI in pigs at baseline and 72 h after I/R surgery ($n = 5$). **I** Gross pathological images of heart sections (bar = 1 cm) and quantification of the scar area ($n = 5$). **J** Representative electron microscopy images (20,000×) of heart sections from pigs 4 weeks after I/R surgery (bar = 500 nm). **K** Quantification of mitochondrial volume and the number of mitochondria with disorganized cristae ($n = 5$). **L** GO enrichment analysis of the differentially expressed proteins in the hearts of male Bama miniature pigs. Groups were compared via Student's *t*-test (**B**, **I**, and **K**), and 2-way ANOVA and multiple-comparison post hoc analysis (**C**–**H**). Data are presented as the means ± SD (*$P < 0.05$; **$P < 0.01$; ***$P < 0.001$; ****$P < 0.0001$; n.s., not significant)

normal or increased vitamin B12 levels, which cannot be consistently corrected by high-dose B12 supplementation [13, 50]. Consistently, we found that serum B12 increased in parallel with hs-cTnT across the groups of MMA concentrations, although this change did not reach statistical significance. Moreover, myocardial injury was related to serum MMA rather than vitamin B12, which was partly explained by the decrease in *MMUT* expression in heart tissue post-IR. Strikingly, cardiac *MMUT* overexpression delivered by AAV carriers alleviated MMA accumulation, mitochondrial impairment, and heart remodeling in porcine I/R models. Given that HF is one of the major challenges after AMI, we evaluated early infarct area and chronic cardiac remodeling post-I/R via CMR in pigs, and did not perform TTC/Evans blue staining to assess pathological infarct size. Although the estimation of AAR by CMR is controversial, CMR is the primary clinical method for assessing infarct size [51]. Nonetheless, MMUT overexpression alleviated absolute infarct mass and cardiac dysfunction. Indeed, AAV-mediated genome editing and domino liver transplantation, as a form of active *MMUT* supplementation, have been demonstrated to mitigate the neurological symptoms and life expectancy of patients with inborn methylmalonic acidemia [36, 52, 53]. Our preclinical study supports the value of improving mitochondrial MMA metabolism as a promising novel therapeutic approach against I/R injury in male pigs, and future studies need to consider sex.

Mitochondria have emerged as the focal point in the cardioprotection arena because of their crucial involvement in cardiomyocyte fate [42]. Mitophagy is a critical mechanism of mitochondrial quality control underlying the restoration of mitochondrial health in the heart [54]. PINK1/Parkin pathway is the classical pathway of mitophagy. Although methylmalonic acidemia inhibits PINK1/Parkin-mediated mitophagy, leading to the accumulation of impaired mitochondria in kidney tissues [49], this signaling was elevated post-I/R but failed to effectively dispose of damaged mitochondria. *Mmut* knockout inhibited the expression of BNIP3 in heart tissues post-I/R, whereas other mitophagy receptors, including FUNDC1, NIX, and Rab9, were not affected. Mitochondrial quality control operates through a collaborative process. We previously demonstrated that exogenous MMA induced mitochondrial ferroptosis features in vitro [21]. This study revealed that myocardial-specific *Mmut* deficiency exacerbated multidimensional abnormalities in mitochondrial quality control under I/R conditions. BNIP3 overexpression substantially restored mitochondrial quality and cardiac phenotypes in the I/R hearts of *Mmut*-deficient mice. This finding is supported by previous reports that BNIP3 promotes Parkin-mediated mitophagy and Opa1-mediated mitochondrial fragmentation [55]. Some studies have reported conflicting effects of mitochondrial autophagy/mitophagy on cell survival, involving Parkin and BNIP3 [6, 56–59]. This discrepancy may be attributed to an imbalance in mitochondrial assimilation and biogenesis. Focusing on the entirety of mitochondrial quality control rather than individual components is imperative.

Acetylation and deacetylation are recognized as key posttranslational regulators in response to metabolic stress [60]. We identified CREB as a key transcription factor regulating BNIP3 expression and reported a novel acetylation at the K^{309} site, which is distinct from the reported acetylated $K^{91/94/136}$ sites [61]. Overall, the inhibition of SIRT1-mediated $CREB^{K309}$ deacetylation represents a critical upstream signal for MMA-induced impairment of BNIP3-mediated mitochondrial quality control post-I/R. In future studies, the mechanism for the accumulation of MMA and decreased expression of MMUT in I/R hearts requires elucidation. Taken together, these preclinical and clinical findings suggest a role for MMA elevation in I/R-induced dysregulated mitochondrial quality control and myocardial vulnerability compared with its well-known isomers, and provide a rationale for considering MMA metabolism as a potential therapeutic target and prognostic biomarker for patients with AMI.

This study had some limitations. Firstly, relatively small sample sizes and a 1-year follow-up in validated cohorts of AMI patients may constrain the statistical power for evaluating the long-term prognostic value of MMA. Thus, further assessment of MMA as a predictor of HF post-infarction is warranted in large-scale cohorts. Secondly, the therapeutic potential of targeting MMA metabolism was evaluated exclusively in a male porcine model, which limits the generalizability of these preclinical findings to female subjects. Finally, although our study focuses on elucidating the impacts and mechanisms of MMA exacerbating myocardial vulnerability, the upstream mechanisms driving MMA metabolic dysregulation in AMI patients remain to be further investigated.

Conclusions

This study indicates elevated circulating MMA as an independent prognostic biomarker for myocardial vulnerability. Distinct from its isomer succinate, sustained cardiac MMA accumulation exacerbates I/R injury by impairing mitochondrial quality control. Mechanistically, MMA inhibits SIRT1 deacetylase activity, causing CREB hyperacetylation at K309, which blunts its binding to the BNIP3 promoter and represses protective mitophagy. In addition, cardiac MMUT overexpression mitigates MMA

accumulation, reduces infarct size, and improves cardiac function in a preclinical porcine model. These findings establish dysregulated MMA metabolism as a novel pathogenic contributor and a promising therapeutic target for cardioprotection during reperfusion.

Abbreviations

AAR	Area at risk
AAV9	Adeno-associated virus serotype 9
AMI	Acute myocardial infarction
BNIP3	BCL2/adenovirus E1B 19 kDa interacting protein 3
ChIP	Chromatin immunoprecipitation
CMR	Cardiac magnetic resonance
CREB	CAMP response element-binding protein
CVD	Cardiovascular disease
HF	Heart failure
H/R	Hypoxia/reoxygenation
I/R	Ischemia/reperfusion
LAD	Left anterior descending (coronary artery)
LC–MS/MS	Liquid chromatography–tandem mass spectrometry
MMA	Methylmalonic acid
MMUT	Methylmalonyl-CoA mutase (human gene/protein)
Mmut	Methylmalonyl-CoA mutase (mouse gene/protein)
pPCI	Primary percutaneous coronary intervention
PTM	Posttranslational modification
ROS	Reactive oxygen species
SA	Succinate/succinic acid
SIRT1	Sirtuin 1
TTC	Triphenyltetrazolium chloride

Supplementary Information

The online version contains supplementary material available at https://doi.org/10.1186/s12916-025-04596-9.

Additional file 1: Figures S1–S11. Fig. S1. I/R-induced MMA accumulation is independent of oxidative stress. Fig. S2. Exogenous methylmalate and succinate have distinct effects on myocardial injury post-I/R. Fig. S3. Mmut deficiency aggravates myocardial reperfusion injury in female mice. Fig. S4. Endogenous MMA accumulation has nonsignificant effect on cardiac regeneration. Fig. S5. The effect of MMA treatment on acetylproteomics in AC16 cells in vitro. Fig. S6. Characterization of the mitochondrial oxygen consumption rate related to MMA accumulation. Fig. S7. The effect of MMA accumulation on mitochondrial quality control. Fig. S8. BNIP3 overexpression reverses MMA-related myocardial vulnerability by activating mitophagy signals. Fig. S9. Acetylation of CREB may be the primary mechanism regulating the expression of BNIP3. Fig. S10. MMA promotes CREB hyperacetylation via inhibiting SIRT1 activity to hinder BNIP3-mediated mitochondrial quality control. Fig. S11. MMUT overexpression improves methylmalate metabolism and cardiac function in pigs subjected to I/R injury. Tables S1–S8. Table S1. General characteristics of 11,410 participants without a history of cardiovascular disease in cohort 1. Table S2. Baseline characteristics of 49 pairs of AMI patients with or without incident heart failure in cohort 2 for widely targeted metabolomics. Table S3. Baseline characteristics of 150 pairs of STEMI patients with or without incident heart failure in cohort 3 for targeted detection of SA and MMA. Table S4. Echocardiography parameters of cardiac myocyte-specific Mmut knockoutmice compared to those of Mmut flox homozygousmice after I/R injury. Table S5. Echocardiography parameters of sham or cardiac I/R model mice injected with control AAV9 compared with those injected with BNIP3 AAV9. Table S6. Serial cardiac magnetic resonance analyses. Table S7. Sample size calculation. Table S8 Primer sequencesused for RT-qPCR analysis.

Additional file 2. Images of the original gels and blots.

Acknowledgements
We extend our gratitude to all participants involved in the study.

Authors' contributions
SF, SW and BY conceived and designed the study. SW, JG, and ZW developed the protocols. KC, ZW, GM, GW, and LX constructed the large animal study. JG, XL, ZZ and YC contributed to the molecular and biological experiments. YW, HL and SL contributed to the clinical data and blood samples. ZW, ZL and HC contributed to pathology. SW and YW contributed to the statistical analyses and interpretation. SW and JG wrote the manuscript. All authors edited and approved the final version. BY, SF and HJ supervised and took responsibility for the integrity and accuracy of the study. All authors read and approved the final manuscript.

Funding
This work was supported by the National Natural Science Foundation of China (82170262, 81870353, 62135002, 82200396, 82200546, and 82500386) and the Natural Science Foundation of Heilongjiang Province (grant LH2022H024).

Data availability
The data that support the findings of this study are available from the corresponding author upon reasonable request.

Declarations

Ethics approval and consent to participate
The animal experiments were approved by the Second Affiliated Hospital of Harbin Medical University Animal Care and Use Committee (number: KY201902112). The NHANES study (cohort 1) was approved by the research ethics review board of the Centers for Disease Control and Prevention (Protocol No. 98–12). The research in cohort 2 and cohort 3 was approved by the Ethics Committee of Harbin Medical University (KY2017-249) and was performed in accordance with the Declaration of Helsinki.

Consent for publication
Not applicable.

Competing interests
The authors declare no competing interests.

Author details
[1]Department of Cardiology, Second Affiliated Hospital of Harbin Medical University, Harbin, China. [2]The Key Laboratory of Myocardial Ischemia, State Key Laboratory of Frigid Zone Cardiovascular Diseases (SKLFZCD), Harbin, China. [3]Department of Thoracic Surgery, First Affiliated Hospital of Anhui Medical University, Hefei, China. [4]Department of Cardiology, First Affiliated Hospital of Jiamusi University, Jiamusi, China. [5]College of Pharmacy, Heilongjiang Province Key Laboratory of Research On Molecular Targeted Anti-Tumor Drugs, Harbin Medical University, Harbin, China. [6]Department of Neurobiology, Harbin Medical University, Harbin, China.

Received: 14 July 2025 Accepted: 18 December 2025
Published online: 31 December 2025

References

1. Byrne RA, Rossello X, Coughlan JJ, Barbato E, Berry C, Chieffo A, et al. 2023 ESC guidelines for the management of acute coronary syndromes. Eur Heart J. 2023;44(38):3720–826.
2. Ale-Agha N, Jakobs P, Goy C, Zurek M, Rosen J, Dyballa-Rukes N, et al. Mitochondrial telomerase reverse transcriptase protects from myocardial ischemia/reperfusion injury by improving complex I composition and function. Circulation. 2021;144(23):1876–90.
3. Comita S, Femmino S, Thairi C, Alloatti G, Boengler K, Pagliaro P, et al. Regulation of STAT3 and its role in cardioprotection by conditioning: focus on non-genomic roles targeting mitochondrial function. Basic Res Cardiol. 2021;116(1):56.
4. Eldeeb MA, Thomas RA, Ragheb MA, Fallahi A, Fon EA. Mitochondrial quality control in health and in Parkinson's disease. Physiol Rev. 2022;102(4):1721–55.
5. Ai L, de Freitas GJ, Huang C, Aniag M, Sawaged S, Sin J, Thakur R, Rai D, Rainville C, Sterner DE et al: Enhanced Parkin-mediated mitophagy

mitigates adverse left ventricular remodelling after myocardial infarction: role of PR-364. Eur Heart J 2024.
6. Ajoolabady A, Chiong M, Lavandero S, Klionsky DJ, Ren J. Mitophagy in cardiovascular diseases: molecular mechanisms, pathogenesis, and treatment. Trends Mol Med. 2022;28(10):836–49.
7. Forny P, Bonilla X, Lamparter D, Shao W, Plessl T, Frei C, et al. Integrated multi-omics reveals anaplerotic rewiring in methylmalonyl-CoA mutase deficiency. Nat Metab. 2023;5(1):80–95.
8. Wang S, Liu Y, Liu J, Tian W, Zhang X, Cai H, et al. Mitochondria-derived methylmalonic acid, a surrogate biomarker of mitochondrial dysfunction and oxidative stress, predicts all-cause and cardiovascular mortality in the general population. Redox Biol. 2020;37:101741.
9. Keller SA, Luciani A. Mitochondrial distress in methylmalonic acidemia: novel pathogenic insights and therapeutic perspectives. Cells. 2022. https://doi.org/10.3390/cells11193179.
10. Azar MR, Shakiba M, Tafreshi Rl, Rashed MS. Heart failure in a patient with methylmalonic acidemia. Mol Genet Metab. 2007;92(1–2):188.
11. Arhip L, Brox-Torrecilla N, Romero I, Motilla M, Serrano-Moreno C, Miguelez M, et al. Late-onset methylmalonic acidemia and homocysteinemia (cblC disease): systematic review. Orphanet J Rare Dis. 2024;19(1):20.
12. Green R, Allen LH, Bjørke-Monsen A, Brito A, Guéant J, Miller JW, et al. Vitamin B12 deficiency. Nat Rev Dis Primers. 2017;3(1):17040.
13. Wang S, Wang Y, Wan X, Guo J, Zhang Y, Tian M, et al. Cobalamin intake and related biomarkers: examining associations with mortality risk among adults with type 2 diabetes in NHANES. Diabetes Care. 2022;45(2):276–84.
14. Lin L, Hu Y, Lei F, Huang X, Zhang X, Sun T, et al. Cardiovascular health and cancer mortality: evidence from US NHANES and UK Biobank cohort studies. BMC Med. 2024;22(1):368.
15. Tan X, Tang F, Tian W, Zhang Y, Fang S, Yang S, et al. Homocysteine metabolism, subclinical myocardial injury, and cardiovascular mortality in the general population. JACC Asia. 2024;4(8):609–20.
16. Guo J, Liu Y, Liu X, Yan M, Zhang Y, Fang S, et al. Systolic and diastolic blood pressure, cardiac biomarkers, and cardiovascular mortality in adults without cardiovascular disease. JACC Adv. 2025;4(5):101678.
17. Wang Y, Wu P, Chen Z, Li Z, Wang Y, Yan M, Zhang Y, Wang S, Fang S, Yu B: Prognostic value of tryptophan catabolism-base scores in acute myocardial infarction patients. J Adv Res 2025.
18. Cai HX, Liang CC, Wang SJ, Guo JC, Wang Y, Yu B, et al. Renin-angiotensin system antagonists and mortality due to pneumonia, influenza, and chronic lower respiratory disease in patients with hypertension. J Geriatr Cardiol. 2022;19(7):511–21.
19. Bei Y, Zhu Y, Zhou J, Ai S, Yao J, Yin M, et al. Inhibition of Hmbox1 promotes cardiomyocyte survival and glucose metabolism through Gck activation in ischemia/reperfusion injury. Circulation. 2024;150(11):848–66.
20. Mendieta G, Ben-Aicha S, Gutierrez M, Casani L, Arzanauskaite M, Carreras F, et al. Intravenous statin administration during myocardial infarction compared with oral post-infarct administration. J Am Coll Cardiol. 2020;75(12):1386–402.
21. Guo J, Wang S, Wan X, Liu X, Wang Z, Liang C, et al. Mitochondria-derived methylmalonic acid aggravates ischemia-reperfusion injury by activating reactive oxygen species-dependent ferroptosis. Cell Commun Signal. 2024;22(1):53.
22. Wang YP, Sharda A, Xu SN, van Gastel N, Man CH, Choi U, et al. Malic enzyme 2 connects the Krebs cycle intermediate fumarate to mitochondrial biogenesis. Cell Metab. 2021;33(5):1027–41.
23. Cluntun AA, Badolia R, Lettlova S, Parnell KM, Shankar TS, Diakos NA, et al. The pyruvate-lactate axis modulates cardiac hypertrophy and heart failure. Cell Metab. 2021;33(3):629–48.
24. Cui H, Chen Y, Li K, Zhan R, Zhao M, Xu Y, et al. Untargeted metabolomics identifies succinate as a biomarker and therapeutic target in aortic aneurysm and dissection. Eur Heart J. 2021;42(42):4373–85.
25. Gomes AP, Ilter D, Low V, Endress JE, Fernandez-Garcia J, Rosenzweig A, et al. Age-induced accumulation of methylmalonic acid promotes tumour progression. Nature. 2020;585(7824):283–7.
26. Tang F, Yan M, Wang Z, Chen Z, Liu Y, E M, et al. Mitochondrial metabolite methylmalonic acid, subclinical myocardial injury, and its incremental predictive value for cardiovascular mortality risk. Arch Med Res. 2025;56(6):103226.
27. Liu Y, Gao Y, Liu Y, Zhang Y, Wang S, Yu B. Prevalence of functional cobalamin deficiency and relevant mortality risk in the general population: an unheeded phenotype distinct from cobalamin deficiency. J Am Nutr Assoc. 2025;44(3):181–9.
28. Wang S, Chen K, Wang Y, Wang Z, Li Z, Guo J, et al. Cardiac-targeted delivery of nuclear receptor RORalpha via ultrasound targeted microbubble destruction optimizes the benefits of regular dose of melatonin on sepsis-induced cardiomyopathy. Biomater Res. 2023;27(1):41.
29. Batkai S, Genschel C, Viereck J, Rump S, Bar C, Borchert T, et al. CDR132L improves systolic and diastolic function in a large animal model of chronic heart failure. Eur Heart J. 2021;42(2):192–201.
30. Santos-Gallego CG, Requena-Ibanez JA, San AR, Ishikawa K, Watanabe S, Picatoste B, et al. Empagliflozin ameliorates adverse left ventricular remodeling in nondiabetic heart failure by enhancing myocardial energetics. J Am Coll Cardiol. 2019;73(15):1931–44.
31. Zhang X, Duan Y, Zhang X, Jiang M, Man W, Zhang Y, et al. Adipsin alleviates cardiac microvascular injury in diabetic cardiomyopathy through Csk-dependent signaling mechanism. BMC Med. 2023;21(1):197.
32. Cai W, Liu L, Shi X, Liu Y, Wang J, Fang X, et al. Alox15/15-HpETE aggravates myocardial ischemia-reperfusion injury by promoting cardiomyocyte ferroptosis. Circulation. 2023;147(19):1444–60.
33. Jin L, Geng L, Ying L, Shu L, Ye K, Yang R, et al. FGF21-sirtuin 3 axis confers the protective effects of exercise against diabetic cardiomyopathy by governing mitochondrial integrity. Circulation. 2022;146(20):1537–57.
34. Yan P, Li Z, Xiong J, Geng Z, Wei W, Zhang Y, et al. LARP7 ameliorates cellular senescence and aging by allosterically enhancing SIRT1 deacetylase activity. Cell Rep. 2021;37(8):110038.
35. Tahir UA, Katz DH, Avila-Pachecho J, Bick AG, Pampana A, Robbins JM, et al. Whole genome association study of the plasma metabolome identifies metabolites linked to cardiometabolic disease in black individuals. Nat Commun. 2022;13(1):4923.
36. Venturoni LE, Chandler RJ, Liao J, Hoffmann V, Ramesh N, Gordo S, et al. Growth advantage of corrected hepatocytes in a juvenile model of methylmalonic acidemia following liver directed adeno-associated viral mediated nuclease-free genome editing. Mol Genet Metab. 2022;137(1–2):1–8.
37. Narita T, Weinert BT, Choudhary C. Functions and mechanisms of non-histone protein acetylation. Nat Rev Mol Cell Biol. 2019;20(3):156–74.
38. Morita M, Naito Y, Yoshikawa T, Niki E. Plasma lipid oxidation induced by peroxynitrite, hypochlorite, lipoxygenase and peroxyl radicals and its inhibition by antioxidants as assessed by diphenyl-1-pyrenylphosphine. Redox Biol. 2016;8:127–35.
39. Li B, Liu F, Chen X, Chen T, Zhang J, Liu Y, et al. FARS2 deficiency causes cardiomyopathy by disrupting mitochondrial homeostasis and the mitochondrial quality control system. Circulation. 2024. https://doi.org/10.1161/CIRCULATIONAHA.123.064489.
40. Shao D, Kolwicz SJ, Wang P, Roe ND, Villet O, Nishi K, et al. Increasing fatty acid oxidation prevents high-fat diet-induced cardiomyopathy through regulating parkin-mediated mitophagy. Circulation. 2020;142(10):983–97.
41. Shaw J, Kirshenbaum LA. Molecular regulation of autophagy and apoptosis during ischemic and non-ischemic cardiomyopathy. Autophagy. 2008;4(4):427–34.
42. Zuccolotto DRF: Mitochondria and the heart. Eur Heart J 2024.
43. Chouchani ET, Pell VR, Gaude E, Aksentijevic D, Sundier SY, Robb EL, et al. Ischaemic accumulation of succinate controls reperfusion injury through mitochondrial ROS. Nature. 2014;515(7527):431–5.
44. Martin JL, Costa A, Gruszczyk AV, Beach TE, Allen FM, Prag HA, et al. Succinate accumulation drives ischaemia-reperfusion injury during organ transplantation. Nat Metab. 2019;1:966–74.
45. Dodd MS, Sousa FM, Montes AC, Kerr M, Timm KN, Griffin JL, et al. Fatty acids prevent hypoxia-inducible factor-1alpha signaling through decreased succinate in diabetes. JACC Basic Transl Sci. 2018;3(4):485–98.
46. Prag HA, Gruszczyk AV, Huang MM, Beach TE, Young T, Tronci L, et al. Mechanism of succinate efflux upon reperfusion of the ischaemic heart. Cardiovasc Res. 2021;117(4):1188–201.
47. Dhar I, Lysne V, Ulvik A, Svingen G, Pedersen ER, Bjornestad EO, et al. Plasma methylmalonic acid predicts risk of acute myocardial infarction and mortality in patients with coronary heart disease: a prospective 2-cohort study. J Intern Med. 2023;293(4):508–19.
48. Lakso HA, Appelblad P, Schneede J. Quantification of methylmalonic acid in human plasma with hydrophilic interaction liquid chromatography separation and mass spectrometric detection. Clin Chem. 2008;54(12):2028–35.

49. Luciani A, Schumann A, Berquez M, Chen Z, Nieri D, Failli M, et al. Impaired mitophagy links mitochondrial disease to epithelial stress in methylmalonyl-CoA mutase deficiency. Nat Commun. 2020;11(1):970.
50. Tang F, Qiu H, Liu Y, Guo J, Huang Z, Fang S, et al. Decreased cobalamin sensitivity and biological aging acceleration in the general population. J Nutr Health Aging. 2024;28(7):100262.
51. Heusch P, Nensa F, Heusch G. Is MRI really the gold standard for the quantification of salvage from myocardial infarction? Circ Res. 2015;117(3):222–4.
52. An D, Frassetto A, Jacquinet E, Eybye M, Milano J, DeAntonis C, et al. Long-term efficacy and safety of mRNA therapy in two murine models of methylmalonic acidemia. EBioMedicine. 2019;45:519–28.
53. Chakrapani A, Stojanovic J, Vara R, De Nictolis F, Spada M, Dionisi-Vici C. Safety, efficacy, and timing of transplantation(s) in propionic and methylmalonic aciduria. J Inherit Metab Dis. 2023;46(3):466–81.
54. Picca A, Mankowski RT, Burman JL, Donisi L, Kim JS, Marzetti E, et al. Mitochondrial quality control mechanisms as molecular targets in cardiac ageing. Nat Rev Cardiol. 2018;15(9):543–54.
55. Wang S, Long H, Hou L, Feng B, Ma Z, Wu Y, et al. The mitophagy pathway and its implications in human diseases. Signal Transduct Target Ther. 2023;8(1):304.
56. Song M, Gong G, Burelle Y, Gustafsson AB, Kitsis RN, Matkovich SJ, et al. Interdependence of parkin-mediated mitophagy and mitochondrial fission in adult mouse hearts. Circ Res. 2015;117(4):346–51.
57. Schmid ET, Pyo JH, Walker DW. Neuronal induction of BNIP3-mediated mitophagy slows systemic aging in *Drosophila*. Nat Aging. 2022;2(6):494–507.
58. Cho YK, Son Y, Saha A, Kim D, Choi C, Kim M, et al. STK3/STK4 signalling in adipocytes regulates mitophagy and energy expenditure. Nat Metab. 2021;3(3):428–41.
59. Li Y, Liang P, Jiang B, Tang Y, Liu X, Liu M, et al. CARD9 promotes autophagy in cardiomyocytes in myocardial ischemia/reperfusion injury via interacting with Rubicon directly. Basic Res Cardiol. 2020;115(3):29.
60. Shimazu T, Hirschey MD, Newman J, He W, Shirakawa K, Le Moan N, et al. Suppression of oxidative stress by beta-hydroxybutyrate, an endogenous histone deacetylase inhibitor. Science. 2013;339(6116):211–4.
61. Steven A, Friedrich M, Jank P, Heimer N, Budczies J, Denkert C, et al. What turns CREB on? And off? And why does it matter? Cell Mol Life Sci. 2020;77(20):4049–67.

Publisher's Note

Springer Nature remains neutral with regard to jurisdictional claims in published maps and institutional affiliations.